UC San Diego

UC San Diego Electronic Theses and Dissertations

Title

Reduced Thermal Conductivity of Compacted Silicon Nanowires

Permalink

https://escholarship.org/uc/item/3rs950vx

Author

Yuen, Taylor S.

Publication Date

2013

Peer reviewed|Thesis/dissertation

eScholarship.org Powered by the California Digital Library
University of California

UNIVERSITY OF CALIFORNIA, SAN DIEGO

Reduced Thermal Conductivity of Compacted Silicon Nanowires

A Thesis submitted in partial satisfaction of the requirements
for the degree Master of Science

in

Materials Science and Engineering

by

Taylor S. Yuen

Committee in charge:

Professor Renkun Chen, Chair
Professor Prabhakar R. Bandaru
Professor Joe Goddard

2013

The Thesis of Taylor S. Yuen is approved, and it is acceptable in quality and form for publication on microfilm and electronically:

Chair

University of California, San Diego

2013

DEDICATION

To my parents, Bessie and Dexter Yuen,

for their loving support and encouragement during my Master's program.

EPIGRAPH

"'FOR I KNOW THE PLANS I HAVE FOR YOU', DECLARES THE LORD. 'PLANS TO PROSPER YOU AND NOT TO HARM YOU, PLANS TO GIVE YOU HOPE AND A FUTURE.'"

JEREMIAH 29:11

TABLE OF CONTENTS

Signature Page…… iii

Dedication…… iv

Epigraph……..……. v

Table of Contents…… vi

List of Symbols..…… viii

List of Figures..…… xi

List of Tables…….xiv

Acknowledgements……....xv

Abstract…… xvi

Introduction ……..…… 1

Chapter 1: Heat Conduction in Nanostructured Materials
1.1: Limitations of Classical Heat Transfer ……. 3
1.2: Heat Carriers ……. 4
1.3: Nanoscale Heat Transfer Processes ….……. 7
1.4: Size-Effects of Nanostructures on Heat Transfer ….…...……10
1.5: Thermal Boundary Resistance……. ….…...……... 13

Chapter 2: Examples of Reduced Thermoconductivity in Nanostructued Materials
2.1: Nanowires……... 17
2.2:Superlattices……..…19
2.3:Nanocomposites……....20

Chapter 3: Fabrication of Compacted Silicon Nanowire Sample
3.1: Glove Box and Oxygen Purifier Set-up……..22
3.2: Hot Press Set-Up…….24
3.3: Sample Preparation……..26
3.4: Sample Characteristics…….29

Chapter 4: Modeling of Thermal Conductivity of Compacted Silicon Nanowires
4.1: Introduction to Analytical Models for the Thermal Conductivity of Compacted Silicon Nanowires……...32

4.2: Effective Thermal Conductivity of Silicon-Silicon Interfaces……..33
4.3: Effective Thermal Conductivity of Porous Medium……..36
4.4: The Analytical Model of the Thermal Conductivity of Compacted Silicon Nanowires……..38
4.5: Monte Carlo Simulation of Phonon Tranport in Compacted Silicon Nanowires …….39

Chapter 5: Measurement of Thermal Conductivity of Compacted Silicon Nanowires
5.1: The 3ω Method……45
5.2: Sample Setup……49
5.3: Results and Discussion...……..…….51

Chapter 6: Conclusions and Future Works...…….. 58

Appendix……60

References …… 69

LIST OF SYMBOLS

a: Crystal Lattice Length

b: Heater Width

C: Specific Heat per Volume of Carriers

c: Speed of Sound

d: Diameter

d_s: Thickness of Sample

F: Shape factor

g : Spring Constant

h: Device Dimension

$\hbar$: Reduced Planck's Constant

I: Current

K: Wave Vector

k: Thermal Conductivity

k_B: Boltzmann Constant

L: Heater Length

m: Mass

N: Density of States

p: Power

P: Porosity

P_s: Scattering Probability

q : Heat Flux

R: Resistance

R_{Bd}: Thermal Boundary Resistance

R_{SiNw}: Thermal Resistance of Silicon Nanowires

S: Seebeck Coefficient

s_i: Intrinsic Scattering Direction

s_r: Interfacial Scattering Direction

∇T: Temperature Gradient

T: Temperature

V: Voltage

V: Volume

v_g: Group Velocity

Z: Acoustic Impedance

α: Coefficient of Transmittance

δ: Thermal Penetration Depth

ε: Shape Factor of Pores

θ: Angle between Direction of Phonon and k Direction

Λ: Mean Free Path

λ: Wave Vector (only for Chapter 5)

ρ: Density

σ: Electrical Conductivity

τ: Relaxation Time

Ψ: Angle between Direction of Phonon and n Direction

φ: Phase Angle

ω: Angular Frequency

LIST OF FIGURES

Figure 1.1: A one-dimensional array of a spring-mass system analogy of phonons…5

Figure 1.2: Phonon dispersion …….6

Figure 1.3: Scattering mechanisms of phonons ……..……..9

Figure 1.4: Vectorial representation of phonon-phonon……...…….9

Figure 1.5: Percentage of thermal conductivity accumulation with respect to mean free path of bulk silicon….……...11

Figure 1.6: Phonon movement in a bulk material and thin film …..…….....12

Figure 1.7: Phonon interactions with interface, reflection and transmission……....13

Figure 2.1: Thermal conductivities of bulk silicon and silicon nanowires……...…17

Figure 2.2: Thermal conductivity of VLS nanowires and porous nanowires with various diameters…….…….....18

Figure 2.3: (Left) Schematic of superlattice. (Right) Comparison of thermal conductivity of bulk GaAs and superlattice GaAs/AlAs with 12x14 periods and 3x3 periods..…….……..... 19

Figure 2.4: Thermal conductivity of $Si_{0.8}Ge_{0.2}$ with respect to temperature. Results are compared to thermal conductivity of RTG……...……..21

Figure 3.1: Schematic of glovebox and oxygen purifier setup…….23

Figure 3.2: Picture of pellet press in glove box during hot pressing procedure……24

Figure 3.3: Picture of induction heater with the oxygen monitor and thermometer….24

Figure 3.4: Front and isometric CAD drawings of the graphite die assembly……..25

Figure 3.5: Close up photo of hot pressing set-up……26

Figure 3.6: Distribution of silicon nanowire diameters……27

Figure 3.7: SEM image of silicon nanowires……...……..…27

Figure 3.8: Picture of nanowire extraction using a razor blade…….28

Figure 3.9: Picture of compacted silicon nanowire sample……...29

Figure 3.10: SEM images of inside of sample…..……..30

Figure 3.11: EDX composition spectrum of the sample..……..……30

Figure 3.12: FIB image of the sample……...31

Figure 4.1: Temperature profile across polycrystalline compound with grains of size d……34

Figure 4.2: Diagram of heat transfer across the silicon nanowire and grain boundaries according to Nan et al. model and Yang et al. model……35

Figure 4.3: Theoretical structure and unit cells of compacted nanowire composites used in Monte Carlo Simulation…….39

Figure 4.4**:** Diagrams of intrinsic scattering event and interfacial scattering event used for Monte Carlo Simulation……42

Figure 4.5**:** a) Normalized temperature distribution in a unit cell of compacted nanocomposite. b) Temperature at Y = 0.5 and Y = 1 indicated by the two dashed lines in (a)……...44

Figure 5.1: Schematic arrangement of the sample for 3ω method……45

Figure 5.2: Schematic of 3ω circuit……...47

Figure 5.3: Sample with heater……..49

Figure 5.4: Gold wire bonded to heater ……50

Figure 5.5: 3ω measurement setup before and after closing the vacuum chamber ...50

Figure 5.6: Initial output of the curve fitting method……53

Figure 5.7: Output of the curve fitting method after adjusting thermal conductivity of Si Nanowire and PMMA……53

Figure 5.8: Thermal conductivity of compacted silicon nanowires and single crystal nanowires……54

Figure 5.9: Experimental thermal conductivity of compacted silicon nanowires compared to Monte Carlo model and analytical model……..55

Figure 5.10: Comparison of thermal conductivity of compacted Si nanowire composite with analytical model (where P = 0)……..56

LIST OF TABLES

Table 3.1: Valves opened and closed during different procedures of the glove box…23

Table A.1: Monte Carlo Simulation of thermal conductivity of compacted Si nanowire composite……64

Table A.2: Measured thermal conductivity of compacted Si nanowire composite…..64

Table A.3: Thermal conductivity of 190 nm Si nanowire and calculated thermal conductivity of compacted Si nanowire composite……65

Table A.4: Thermal conductivity of 115 nm Si nanowire……66

Table A.5: Frequency and V(3w) data…….67

Table A.6: Data for Slope and Matlab Fitting Method……68

ACKNOWLEDGEMENT

The research for this thesis was performed at the University of California, San Diego under the direction of Professor Renkun Chen. I would like to express my deepest gratitude for the guidance he gave me for this project. Without the guidance he gave me, I would not have achieved what I have by the end of this Master's program.

I also would like to thank my colleagues in Chen Laboratory: Jaeyun Moon, Edward Dechaumphai, and Matt Wingert for their help and friendship through the research. Without their help and expertise, I would not have been able to complete this thesis. I thank Jaeyun for her help in creating the fabrication process for the compacted silicon nanowire sample. I thank Edward for helping me with the modeling and measuring of the thermal conductivity of the sample. I thank Matt for taking the FIB images of the sample.

I also thank Zhelin Sun of Xiang Laboratory at the University of California for synthesizing the silicon nanowires for this project. Without his help, I would not have the materials needed to make the sample for this project. I am sincerely thankful for his cooperation for this project.

ABSTRACT OF THE THESIS

Reduced Thermal Conductivity of Compacted Silicon Nanowires

by

Taylor S. Yuen

Master of Science in Materials Science Engineering

University of California, San Diego, 2013

Professor Renkun Chen, Chair

Nanocomposite materials have been sought after because of their reduced thermal conductivity. Nanocomposites are fabricated by compacting nanostructured materials (i.e. nanoparticles, nanowires, etc.) into bulk composites. The reduction in thermal conductivity is attributed to increased thermal boundary resistance at the interfaces between individual nanostructures in the composite. This resistance is attributed to the scattering of phonons at the nanostructure interfaces, as described by the diffuse mismatch model.

This thesis is concerned with the reduced thermal conductivity of compacted silicon nanowires. Reduced thermal conductivity of compacted silicon nanowires has been predicted through first-principles modeling. This treatise will present analytical and computer modeling and experimental results for the thermal conductivity of compacted silicon nanowires.

Introduction

Low thermal conductivity materials have been sought after for several applications. One such application is thermal barrier coatings. The designing of high efficiency engines raises the challenge of finding coatings that can allow the engines to maintain a high operating temperature[1]. These coatings can be applied to the turbine blades of heat engines to reduce the amount of heat wasted by the engine. Such thermal barrier coatings require materials that have low thermal conductivities.

Another area where low thermal conductivity materials are needed is thermoelectric generation. Thermoelectric generators are capable of extracting waste heat from conventional power generators and converting it into usable electrical energy. This conversion of thermal energy into electrical energy is known as the Seebeck effect, which refers to the generation of an electric current due to the temperature gradient in the material. The thermoelectric efficiency of a material depends on its thermoelectric figure of merit, expressed as $ZT = \frac{S^2 \sigma T}{k}$. A major part of increasing the ZT of thermoelectric materials is to reduce the thermal conductivity[2-4].

Low thermal conductivity materials are typically found among ceramics and composite materials. Advances in the synthesis of nanostructured materials have given rise to materials with lower thermal conductivities than bulk materials. This has broadened the range of materials that can be selected for low thermal conductivity applications.

This thesis will focus on the reduced thermal conductivity of compacted silicon nanowires. The thesis will be divided into the following chapters. Chapter 1 will cover the fundamentals of heat transfer in nanostructured materials. Chapter 2 shows examples of synthetic nanostructured materials with reduced thermal conductivity. Chapter 3 presents the experimental setup and fabrication technique used to create a compacted silicon nanowire sample. Chapter 4 reviews the theoretical modeling used to predict the thermal conductivity of compacted silicon nanowires. Chapter 5 presents the measurement method used to measure the thermal conductivity of the sample and the results of the measurements. Chapter 6 will contain concluding remarks on the research findings.

Chapter 1: Heat Conduction in Nanostructured Materials

1.1 – Limitations of Classical Heat Transfer

Classical heat transfer studies of conductive heat transfer show that the flow of thermal energy in a material is a result of a temperature gradient. This flow has been described as a diffusion of energy within the material, expressed by the Fourier equation:

$$q = -k\nabla T \tag{1.1}$$

This equation states that the heat flux through the material is proportional to the temperature gradient with a constant of proportionality known as the thermal conductivity, k. The Fourier equation effectively describes heat conduction in bulk materials. However, studies of heat transfer in nanostructured materials have shown lower thermal conductivity than those measured for bulk materials. This is because the Fourier equation has assumed the thermal conductivity of bulk materials to be a material constant, and did not consider the motions of the atoms or electrons during heat conduction. Thermal conductivity measurements of silicon nanowires have demonstrated that their thermal conductivity can be reduced by one to three orders of magnitude from that of bulk silicon depending on the diameter of the nanowires. In order to understand the effects of nanostructures on thermal conductivity, one must look closer into the mechanisms of heat transport in materials

1.2 – Heat Carriers

The mechanism behind heat conduction is the transport of heat by heat carriers. There are two types of carriers involved in conductive heat transport: electrons and phonons. Weakly bounded valence electrons are said to move freely in a solid, serving as energy carriers through the solid[2-4]. Phonons are the lattice vibrations in the crystal structure of material, which occur when thermal energy is applied to the crystal lattice, causing excitations in the lattice structure. Like electrons, phonons have both wave-like and particle-like properties. Both electrons and phonons are excited by thermal energy and in turn "carry" the excess energy through the solid.

Heat conduction in metals is dominated by electrons while heat conduction in insulators and semiconductors is dominated by phonons[2-4,6]. Since this treatise will mostly cover semiconducting materials, further explanation of the nature of phonons is required. As said earlier, phonons exhibit both wave-like and particle-like properties. The wave-like properties of phonons can be visualized using simple mass and spring analogies[2-5]. Imagine the atoms of the crystal lattice being spherical masses connected to each other by springs of length *a* (crystal lattice length). For simplicity, let us consider only a one-dimensional array of masses and springs (see figure 1.1), where all the masses and springs between them are the same.

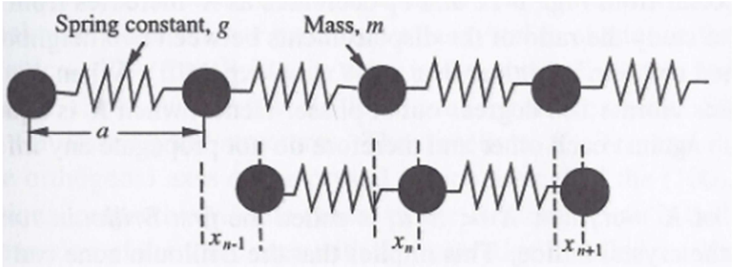


Figure 1.1: A one-dimensional array of a spring-mass system analogy of phonons[2].

If the nth atom is displaced by a distance x_n, the equation of motion can be written as:

$$m * \left(\frac{d^2x}{dt^2}\right) = g * (x_{n+1} + x_{n-1} - 2x_n) \quad (1.2)$$

In this equation, the force on the nth atom is assumed to be contributed only by its nearest neighboring atoms. The solution of this equation should have the form:

$$x_n = x_0 e^{-i\omega t} e^{inKa} \quad (1.3)$$

When this solution is plugged into equation 2.2, the resulting expression is:

$$\omega^2 m = g[2 - e^{-iKa} - e^{iKa} = 2g(1 - \cos Ka) \quad (1.4)$$

$$\omega = \sqrt{\frac{2g}{m}(1 - \cos Ka)}$$

The above equation can be plotted in a ω-K plot (figure 1.2) to show the phonon dispersion.

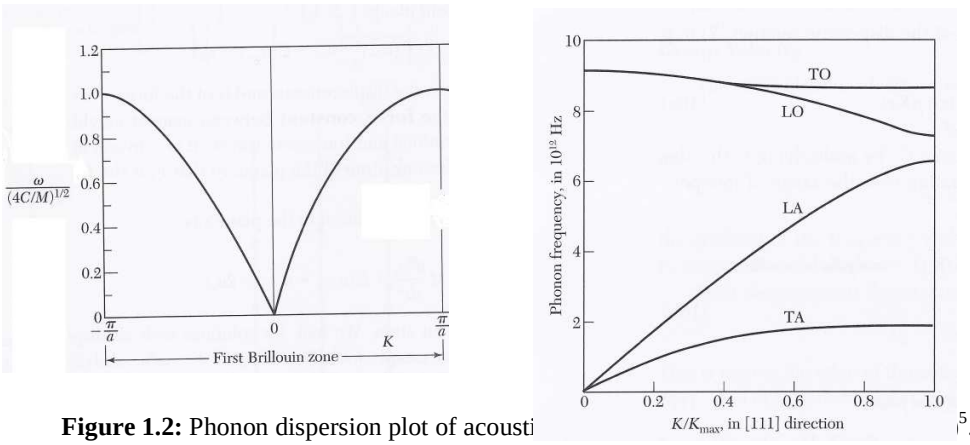


Figure 1.2: Phonon dispersion plot of acousti [5].

The plot of this equation represents the acoustic branch of phonons. Because the crystal lattice of materials is a periodic array, with atoms having a periodicity of a, the minimum allowable wavelength is $2a$. This means that the range of K is $-\frac{\pi}{a}$ to $\frac{\pi}{a}$. The slope of the phonon dispersion is known as the group velocity, v_g, of the phonons (the velocity of energy propagation in a medium). What can also be observed in the phonon dispersion is that the slope of the curve as $K \rightarrow 0$ is constant[2]. This refers to the long-wavelength limit of the phonons and the dispersion relationship (1.4) in this limit can be written as

$$\omega = \sqrt{\frac{g}{m}} Ka = v_g K \qquad (1.5)$$

which is known as the Debye model. The v_g of phonons at the long-wavelength limit is equivalent to the solid medium's speed of sound, hence the name acoustic branch. The long-wavelength limit behavior is typically observed for phonons propagating at low temperatures. Another observation is that as $K \rightarrow \frac{\pi}{a}$,

$v_g \rightarrow 0$. This means that phonons propagating with higher K (or shorter wavelengths) contribute very little to heat conduction. The frequency at the limit $K \rightarrow \frac{\pi}{a}$ is known as the Debye cut-off frequency, $\omega_{D,}$ and is the maximum frequency of the phonon dispersion[2].

The wave motions of phonons can be further analyzed by examining lattices with adjacent atoms having the same spring constants but different masses, or the same masses but different spring constants. This produces a second dispersion curve known as the optical branch (O branches in figure 1.2). The optical branch contains phonons that are propagated when photons (or electromagnetic waves) come into contact with the surface of the solid. Yet, the optical branch phonons have very low group velocities, meaning that they contribute little to heat conduction. One could also consider the transverse and longitudinal motions of the phonons, giving rise to three polarizations of the acoustic branch (one LA, and two TA) and two polarizations of the optical branch (LO and TO) (see figure 1.2). Each of these polarizations or modes of phonon branches can be distinct depending on the crystal orientation of the material.

1.3 – Nanoscale Heat Transfer Processes

When studying heat transfer in nanoscale materials, one must analyze the interactions of carriers within a solid. There are two types of interactions involved in heat transport: carrier-carrier interactions and carrier-defect interactions. These interactions are also known as scattering mechanisms, meaning that these interactions

can cause changes in the wave frequency or direction of the heat carriers. There are two types of scattering: elastic and inelastic scattering. Elastic scattering changes the direction of the heat carriers without changing their frequencies, while inelastic scattering changes the frequencies as well as the direction of the heat carriers[2].

In metallic materials, electrons dominate heat transfer in solids. The main scattering mechanisms are electron-electron scattering, electron-phonon scattering, and electron-defect scattering. It is assumed that electrons are infrequently scattered by other electrons, and hence electron-electron scattering plays only a minor role in heat transfer[3]. Electron-phonon scattering occurs between electrons and acoustic phonons, and electrons and optical phonons. When electrons are scattered by acoustic phonons, their frequencies are not significantly changed, though their direction and momentum is changed (elastic scattering)[2]. When electrons are scattered by optical phonons, the exchange of energy during the process can significantly change their frequencies in addition to changing their direction and momentum (inelastic scattering)[2]. Electron-defect scattering results in the change of direction and momentum of the electrons, but not their frequencies (elastic scattering)[2].

In semiconducting and insulating materials, phonons dominate as heat carriers. Phonon scattering can be divided into three categories: phonon-defect, phonon-electron (mentioned in previous paragraph), and phonon-phonon scattering. Phonon-defect scattering includes phonon-impurity, phonon-dislocation, and phonon-boundary interactions. The frequencies of the phonons remain unchanged during this scattering process (elastic scattering)[2].

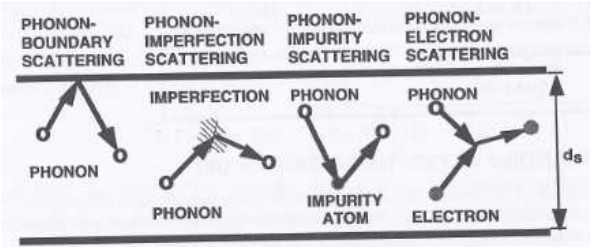


Figure 1.3: Elastic scattering mechanisms of phonons[2].

Phonon-phonon scattering is an inelastic process that changes the energy or frequency of the phonons. There are two types of phonon-phonon scattering processes: normal process and Umklapp process. The normal process scattering occurs when two phonons merge to form a single phonon (case A), or when a single phonon splits into two phonons (case B). In both cases, the frequencies of the phonon changes, but not the momentum, which result in almost no thermal resistance in the material[5]. The Umklapp process occurs when two phonons collide and produce a phonon that has a lower frequency and wave vector, K (case C). The momentum of the phonon is not conserved, contributing to thermal resistance in the material[5].

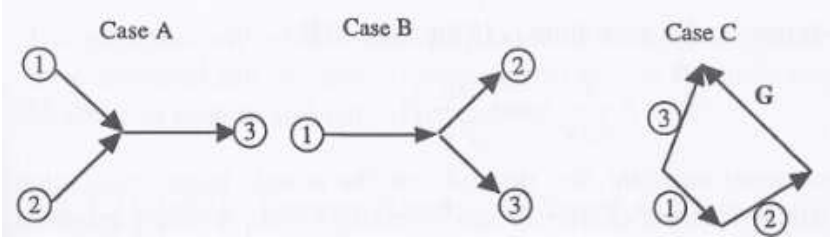


Figure 1.4: Vectorial representation of phonon-phonon scattering. Case A and B represent the normal processes, while case C represents Umklapp process[2].

The scattering mechanisms mentioned are the fundamental means by which heat is transferred within a material, and are essential to understanding heat transfer

within a nanostructured material. Although both elastic and inelastic scattering can contribute to thermal resistance, how much they contribute depends on their effect on the heat carriers. In general, scattering processes that change the direction of the heat carriers against the heat flux or change the momentum of the heat carriers will contribute to thermal resistance.

Scattering mechanisms can be quantified using the relaxation time, τ. τ is described as the average time between collisions[2]. Shorter τ means more scattering occurs. There are different expressions used to calculate τ based on the type scattering that occurs. It is convenient to express the combination of all the scattering mechanisms in a material as the effective relaxation time, τ_{eff}. An assumption often used is the Matthiessen rule, which adds up the scattering rates or the reciprocal of the relaxation times (defect: τ_d; Umklapp: τ_U; boundary: τ_b) for different scattering processes as:

$$\frac{1}{\tau_{eff}} = \frac{1}{\tau_d} + \frac{1}{\tau_U} + \frac{1}{\tau_b} \tag{1.6}$$

The equation essentially adds the thermal resistances posed by each scattering process. Thermal resistance is related to the reduction in thermal conductivity of nanoscale materials. Thus the key to reducing conductivity is to increase the scattering of heat carriers in the material.

1.4 – Classical Size-Effect of Nanostructures on Heat Transfer

As mentioned previously, the basis of heat transfer in a medium is the movements and interactions of electron and phonons. One characteristic length scale

used to describe the movement of electrons and phonons is the mean free path, Λ[6-7]. The mean free path is defined as the average distance a heat carrier travels before transferring its excess energy[6]. In other words, the average distance that an electron or phonon can travel before colliding with another particle. This is related to the relaxation time, τ, as $\Lambda = v_g\tau$. Λ can be related to the thermal conductivity, k, of a material by the following expression based on the kinetic theory:

$$k = \frac{1}{3}\sum_{pol}\int C v_g \Lambda \, d\omega \tag{1.6}$$

where C is the heat capacity of the material. This is a generalized expression for thermal conductivity, which considers the frequency dependence of C, v_g, and Λ as well as the different values of C, v_g, and Λ for each polarization of phonons. Different phonon frequencies contribute differently to the thermal conductivity. The contribution of phonons at different frequencies to the thermal conductivity can be visualized through plots such as the thermal conductivity accumulation with respect to mean free path.

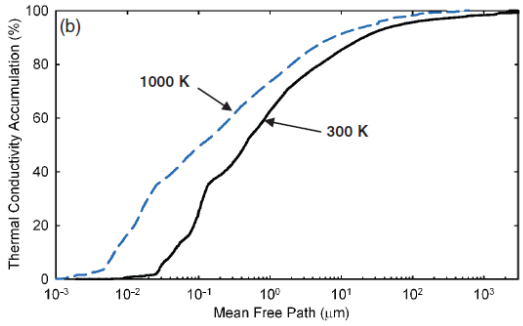


Figure 1.5: Percentage of thermal conductivity accumulation with respect to mean free path of bulk silicon[30].

Figure 1.5 shows that phonons with mean free paths on the order of 100 nm to 1 um greatly contribute to the thermal conductivity of bulk silicon. This infers that phonons at some frequencies contribute more to the thermal conductivity than phonons at other frequencies. In general, low frequency phonons contribute the most to the thermal conductivity.

Another important characteristic length in heat conduction is the device dimension, h, which can be either the diameter or film thickness depending on the structure of the device[6]. In bulk solids, $h >> \Lambda$ which means that scattering occurs far within the solid and a wide spectrum of phonons contribute to the total thermal conductivity[7]. However, if a material is synthesized with $h << \Lambda$ of low frequency phonons, the boundary of the material confines the phonons to have mean free paths that are smaller than low frequency phonons. In essence, this screens out low frequency phonons, which removes their contribution to the thermal conductivity and thus lowers the thermal conductivity. This is known as classical size-effect.

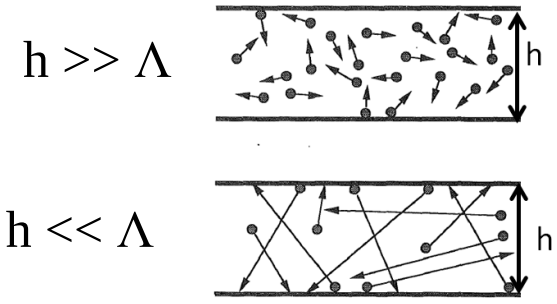


Figure 1.6: Phonon movement in a bulk material (top figure) and thin film (bottom figure). In thin film materials, the mean free paths, Λ, of the phonons are constrained by the size, h[7].

1.5 – Thermal Boundary Resistance

One more aspect that needs to be considered for nanostructured materials is heat transfer at solid-solid interfaces. This is especially important when considering more complex nanostructured materials such as superlattices and nanocomposites (see Chapter 3). In these types of materials, interfaces are formed between dissimilar materials. These can be interfaces between different materials or interfaces of the same material with different crystallographic orientations. The interface can be imaged as a plane in between two dissimilar materials. When phonons come into contact with the interface, they will either reflect off the interface, transmit through the interface, or undergo a combination of both[9]. The occurrence of these events can scatter the phonons and create a resistance to the heat flux known as the thermal boundary resistance.

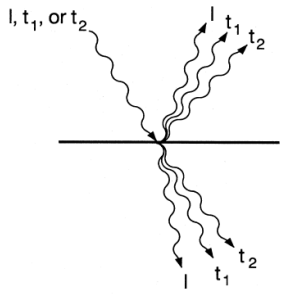


Figure 1.7: Phonon interactions with interface, reflection and transmission.[9]

The heat flux through the interface from material 1 to material 2 can be described by the following expression:

$$q_{1\to2} = \frac{1}{2}\sum_j \int_0^{\frac{\pi}{2}} \int_0^{\omega_{max}} c_{1,j}\hbar\omega\, \mathrm{N}_{1,j}(\omega, \mathrm{T})\alpha_{1\to2}\, \cos\theta \sin\theta\, \mathrm{d}\theta\, \mathrm{d}\omega \qquad (1.7)$$

where $\hbar$ is the reduced Planck's constant, $\mathrm{N}(\omega, \mathrm{T})$ is the phonon density of state, $c_{1,j}$ is the speed of sound for material 1, $\alpha_{1\to2}$ is the transmission coefficient, θ is the incident angle of the phonon, and j is the polarization of the phonons. The expression $\int_0^{\frac{\pi}{2}} \alpha_{1\to2} \cos\theta \sin\theta \, \mathrm{d}\theta$ is known as the transmission probability Γ. The materials at the interface are assumed to be Debye solids with the generalization that the longitudinal and transverse speeds of sound are different, $\mathrm{N}_{1,j}(\omega, \mathrm{T})$ for frequencies below the Debye cutoff frequency, ω_D, is:

$$N_{1,j}(\omega, T) = \frac{\omega^2}{2\pi^2 c_{1,j}^3 [e^{(\frac{\hbar\omega}{k_b \mathrm{T}})} - 1]} \tag{1.8}$$

where k_B is the Boltzmann constant. An expression similar to 1.7 can be made for the heat flux from material 2 to 1. The thermal boundary conductivity can be written as:

$$h_{Bd} = \frac{dq}{dT} = \frac{1}{2} \sum_j \int_0^{\frac{\pi}{2}} \int_0^{\omega_D} c_{1,j} \hbar\omega \, \frac{d\mathrm{N}_{1,j}(\omega,\mathrm{T})}{dT} \alpha_{1\to2,j} \cos\theta \sin\theta \, \mathrm{d}\theta \, \mathrm{d}\omega \tag{1.9}$$

$$h_{Bd} = \frac{1}{4\pi^2} \frac{\hbar^2}{k_b \mathrm{T}^2} \sum_j \int_0^{\frac{\pi}{2}} \int_0^{\omega_D} \frac{\omega^4}{c_{1,j}^2} \frac{e^{(\frac{\hbar\omega}{k_b \mathrm{T}})}}{[e^{(\frac{\hbar\omega}{k_b \mathrm{T}})} - 1]^2} \alpha_{1\to2,j} \cos\theta \sin\theta \, \mathrm{d}\theta \, \mathrm{d}\omega$$

which is the reciprocal of the thermal boundary resistance. The thermal boundary resistance can thus be calculated once the transmission coefficient is determined.

There are two models that have been used to quantify the thermal boundary resistance: the acoustic mismatch model (AMM) and the diffuse mismatch model (DMM). AMM considers all phonons as plane waves traveling through continuous

medium and thermal resistance as the result of differing acoustic properties of the materials at the interface. By assuming that no scattering takes place at the interface, the transmission coefficient, $\alpha_{1\text{-}2}$, for the phonon energy in material 1 incident normal to the interface with material 2 is given as:

$$\alpha_{1\to2} = \frac{4Z_1Z_2}{(Z_1+Z_2)^2} \tag{1.10}$$

where Z = ρc is the acoustic impedance, with *c* and *ρ* being the speed of sound (acoustic phonon velocity) and mass density of the material, respectively. As shown by 1.7, if the materials at the interface are the same, the transmission coefficient is equal to 1. This means that if the materials at the interface are the same, all phonons will transmit through the interface.

DMM assumes that all phonons are diffusely scattered at the interface, and that the phonons striking the interfaces loses "memory" of where they came from[8]. Therefore, the probability of the phonon scattering to one side of the interface is proportional only to the phonon density of states on that side ($\alpha_{1\to2} = 1 - \alpha_{2\to1}$). In addition, the number of phonons leaving material 1 is equal to the number of phonons leaving material 2. Therefore, by balancing the heat flux equations from material 1 and material 2, the transmission coefficient can be derived as:

$$\alpha_{1\to2}(\omega) = \frac{\sum_j c_{2,j}N_{2,j}(\omega,T)}{\sum_j c_{1,j}N_{1,j}(\omega,T)+\sum_j c_{2,j}N_{2,j}(\omega,T)} \tag{1.11}$$

where $N_{1,j}(\omega,T)$ and $N_{2,j}(\omega,T)$ are the phonon density of states on side 1 and 2, respectively. Using the Debye approximation (1.8), 1.11 becomes:

$$\alpha_{1\to2}(\omega) = \frac{\sum_j {c_{2,j}}^{-2}}{\sum_j {c_{1,j}}^{-2}+\sum_j {c_{2,j}}^{-2}} \tag{1.12}$$

According to this model, if the materials at the interface are the same, the transmission coefficient is 0.5. This means that only half of the phonons will be transmitted through the interface even though the materials on each side are the same.

The transmission coefficient calculated by DMM is a factor of 2 lower than the transmission coefficient calculated by AMM. Thus, the thermal boundary resistance calculated by DMM is a factor of 2 higher than that calculated by AMM. It has been observed through experiments that the actual thermal boundary resistance of the interface between two materials is between that calculated by DMM and AMM. In essence, DMM and AMM calculate the upper and lower limits of the thermal boundary resistance, respectively. It is thought that DMM is more appropriate than AMM to model interfacial heat transfer except for the most perfect, epitaxial interfaces between materials[2]. Only for ideal epitaxial interfaces is AMM thought to be more appropriate because of the need to consider coherent reflection at the interface[2].

Chapter 2: Examples of Reduced Thermal Conductivity in Nanostructured Materials

2.1- Nanowires

One way to reduce thermal conductivity in materials is to synthesize nanowires. As noted in chapter 1, if the device dimension of a material is made smaller than the mean free paths of low frequency phonons, the boundary of the material confine the mean free paths to those of high and medium frequency phonons, essentially screening out low frequency phonons. Since low frequency phonons are usually the highest contributors to the thermal conductivity of materials, the thermal conductivity should decrease when these phonons are screened. Nanowires are synthesized with diameters that are smaller than the mean free paths of phonons. Advancements in nanowire synthesis have allowed the synthesis of smaller nanowire diameters such that the nanowires can scatter a wider spectrum of phonons. This leads to larger reductions in the thermal conductivity of silicon (figure 2.1).

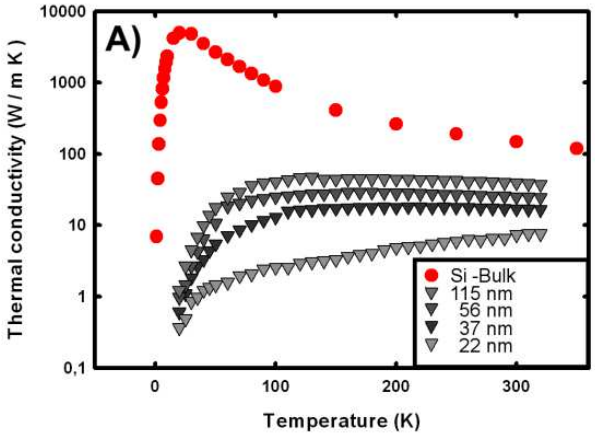


Figure 2.1: Thermal conductivities of bulk silicon and silicon nanowires[32]

In addition, etching pores on the nanowires further increases the scattering of the phonons. This has been synthesized using metal-assisted electroless etching method. One particular method involves etching silicon nanowires on silicon wafers using hydrofluoric acid with silver nitrate[12]. The silver ions in the hydrofluoric acid act as catalysts for the etching of the silicon nanowires, and the etching of micropores on the nanowires. These micropores increase the surface roughness on the nanowires, introducing a secondary phase of scattering[12,13]. The increased scattering at the boundary is said to be due to the increase in the surface to volume ratio of the nanowires. The resulting reduction in the thermal conductivity of these nanowires is shown in the figure below. Although nanowires have provided important insights into classical size-effects on thermal conductivity of nanomaterials, scaling up nanowires for thermal engineering based application would be difficult.

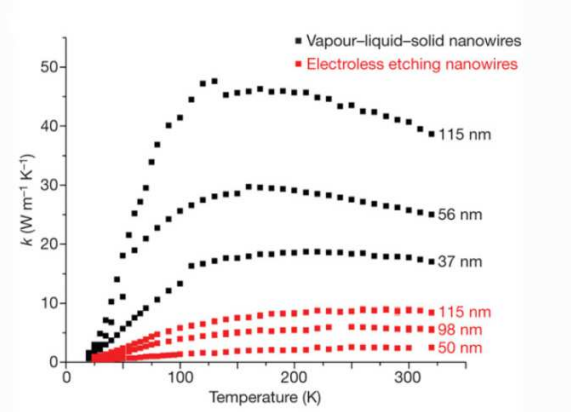


Figure 2.2: Thermal conductivity of VLS nanowires (black) and porous nanowires (red) with various diameters[12].

2.2 - Superlattices

Another attempt to reduce thermal conductivity has been made through the creation of superlattice materials[14]. Superlattices are thin films fabricated by layering two types of materials (such as GaAs/AlAs) in alternating layers of nanoscale thickness. The nanoscale thickness is designed to confine the phonon mean free paths through classical size-effects and thus reduce the thermal conductivity. The nanostructure consists of periodic layers of two materials with different thermal properties. This structure is fabricated to create a series of thermal boundary resistances at the interfaces of each layer in order to further reduce the thermal conductivity of the material[14,15].

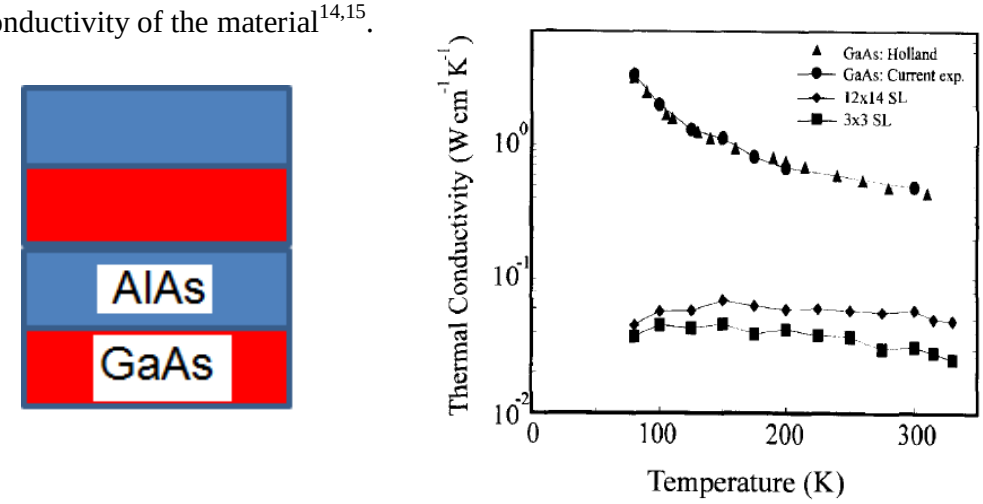


Figure 2.3: (Left) Schematic of superlattice. (Right) Comparison of thermal conductivity of bulk GaAs and superlattice GaAs/AlAs with 12x14 periods and 3x3 periods.

The resistance can be attributed to the scattering of phonons at the interfaces, as described by the diffuse mismatch model. However, coherent reflection and transmission of phonons at the interface, as described by the acoustic mismatch model must also be considered when analyzing the thermal boundary resistance of

superlattices[2,14,15]. Recent research has shown that the phase of low frequency phonons in superlattices seem to be preserved despite the presence of interfaces, thus they are thus transmitted coherently through the superlattice[15]. This allows the low frequency phonons to conduct a considerable fraction of heat through the material, thus resulting in a nearly linear dependence of thermal conductivity on the total superlattice thickness. Therefore, although the thermal conductivity of the superlattice is certainly much lower than the bulk thermal conductivities of the individual materials, the coherent transmission of these low frequency phonons limits the reduction of thermal conductivity, especially when increasing the thickness of the superlattice. In addition, scaling up ordered structures like superlattices for thermal engineering applications would also be very difficult and costly.

2.3 - Nanocomposites

Experimental and theoretical studies on heat conduction mechanisms suggest that an ordered superlattice structure is neither necessary nor optimal for reducing thermal conductivity[16]. Random nanostructures with high interface densities can lead to a reduction in phonon thermal conductivity similar to that in superlattices. This also provides a possibility of scaling up these nanosized structures into bulk size materials for thermal engineering applications.

Nanocomposites are fabricated by compacting nanostructured materials into bulk composites. The reduction in thermal conductivity is attributed to an increase in diffusive scattering at the interfaces between individual nanostructures in the

composite. Reduced thermal conductivity has been demonstrated experimentally for different compacted nanoparticles such as compacted $Si_{0.8}Ge_{0.2}$[16]. The low thermal conductivity of compacted $Si_{0.8}Ge_{0.2}$ compared to the reference radioisotope thermoelectric generator (RTG) sample in the figure below.

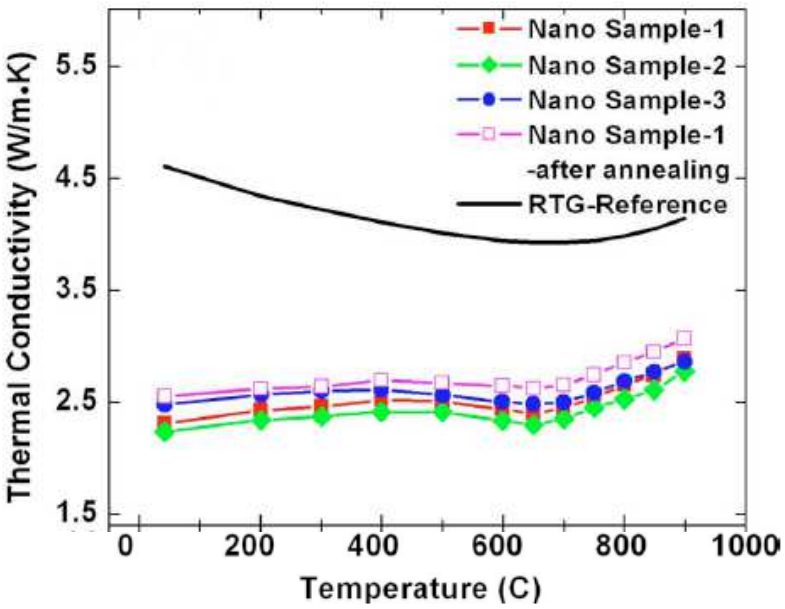


Figure 2.4: Thermal conductivity of $Si_{0.8}Ge_{0.2}$ with respect to temperature[16].

Nanocomposites open a new path to reducing thermal conductivity in materials by introducing nanostructures in bulk size materials. Until recently, the study of nanocomposites was restricted to compacted nanoparticles. It is of great interest to see the effects of compacting other forms of nanostructures into bulk nanocomposities. The results of compacting silicon nanowires will be discussed for the next three chapters.

Chapter 3: Fabrication of Compacted Silicon Nanowires

3.1 – Glove Box and Oxygen Purifier Setup

The compacted silicon nanowires sample examined in this paper was made using a DC induction heating hot pressing procedure. The procedure was conducted in an argon environment within a glove box. Oxygen was purged from the glove box by vacuuming the air in the glove box using the vacuum pump and filling the box with argon gas. When moving items into the glove box via the transfer chamber, the transfer chamber was first purged using a similar procedure as the glove box purge.

After purging the glove box of oxygen, the purified air was circulated from the glove box to an oxygen purifier to maintain an inert environment (O_2 level: ~ 60 ppm). An oxygen monitor was connected to the glove box to measure the oxygen concentration within the glove box. If the oxygen level rose past 300 ppm, the oxygen purifier was regenerated. This was done by heating the oxygen purifier to 500 C and then flowing H_2/N_2 gas through the oxygen purifier. The gas reacted with the oxygen absorbed on FeCl catalysts in the oxygen purifier to produce water vapors, which were then vented out of the purifier into the exhaust pipes. After the regeneration process, the remaining hydrogen gas was vented out of the oxygen purifier using the vacuum pump. A schematic of the setup is shown in the figure below along with a table indicating the valves opened during each glove box procedure.

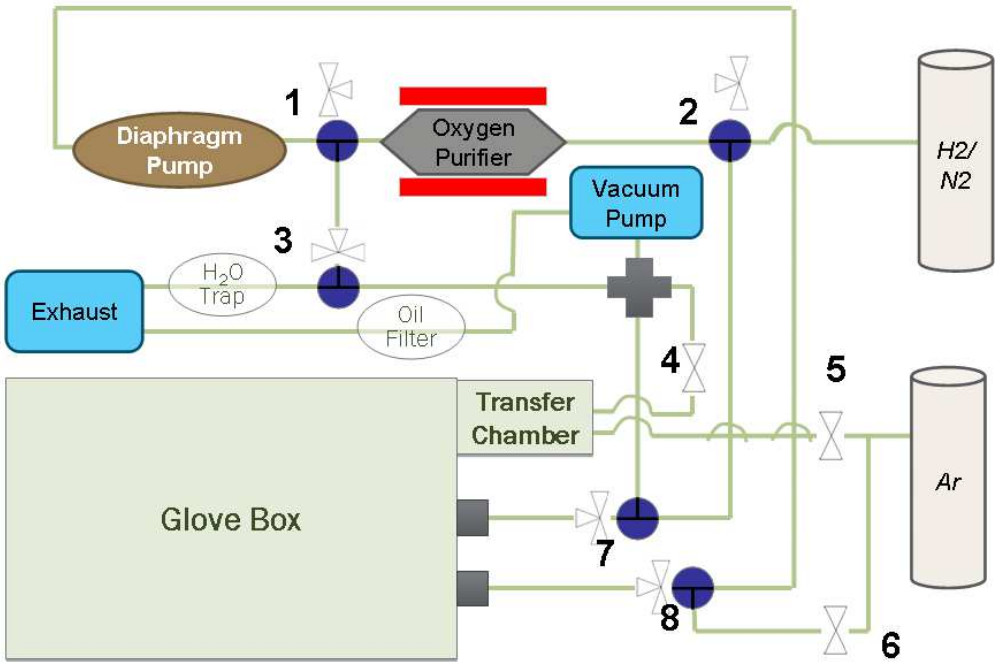


Figure 3.1: Schematic of glovebox and oxygen purifier setup.

Table 3.1: Valves opened (O) and closed (X) during different procedures of the glove box. For three-way valves (1,2,3,7,8), the two opened positions are identifies as left (OL) and right (OR).

Valves	Glove box Purging	Transfer Chamber Purging	Circulation to Oxygen Purifier	Oxygen Purifier Regeneration	Hydrogen Removal
1	X	X	OL	OR	OR
2	X	X	X	OR	X
3	X	X	X	OL	OR
4	X	O	X	X	X
5	X	O	X	X	X
6	O	X	X	X	X
7	OL	X	OR	X	X
8	OL	X	OR	X	X

3.2 – Hot Press Setup

The hot pressing procedure involved a DC induction heater and a pellet press. The pellet press was placed inside the glove box, and the coil of the DC induction heater was passed through the wall of the glove box until it was suspended within the pellet press. A radiation shield was placed around the pellet press to keep the heat localized inside the pellet press in order to reach high temperatures.

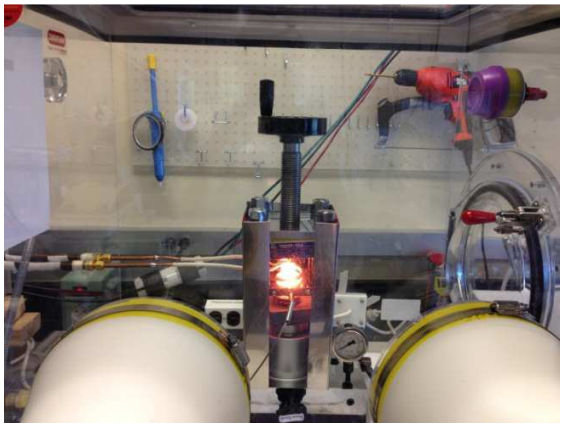


Figure 3.2: Picture of pellet press in glove box during hot pressing procedure.

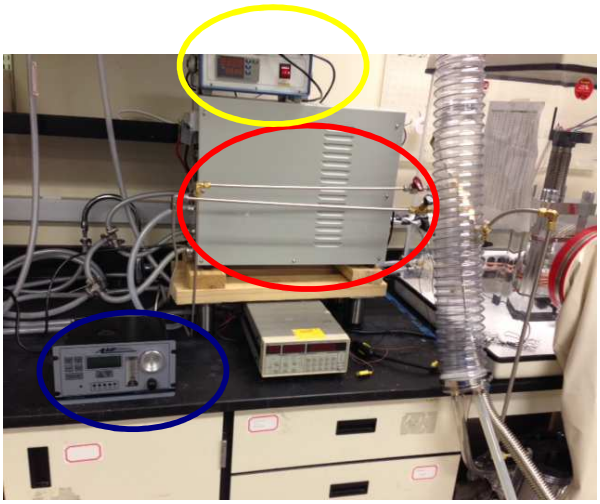


Figure 3.3: Picture of induction heater (red circle) with the oxygen monitor (blue circle) and thermometer (yellow circle).

During a hot pressing procedure, the sample powder would be placed in the graphite die between two graphite spacers (6.35 mm dia., 3 mm thickness) and two alumina rods, with the long rod on top and the short rod on the bottom (long rod: 35 mm, 6.35 mm dia.; short rod: 25 mm, 6.35 mm dia.). The die used for this procedure was a graphite die surrounded by a nickel shell (Alloy HX, McMaster-Carr). The graphite die had an ID of 6.35 mm and an OD of 12.7 mm and the nickel shell had an ID of 12.7 mm and OD of 25.4 mm. The assembly is shown in figure 3.4.

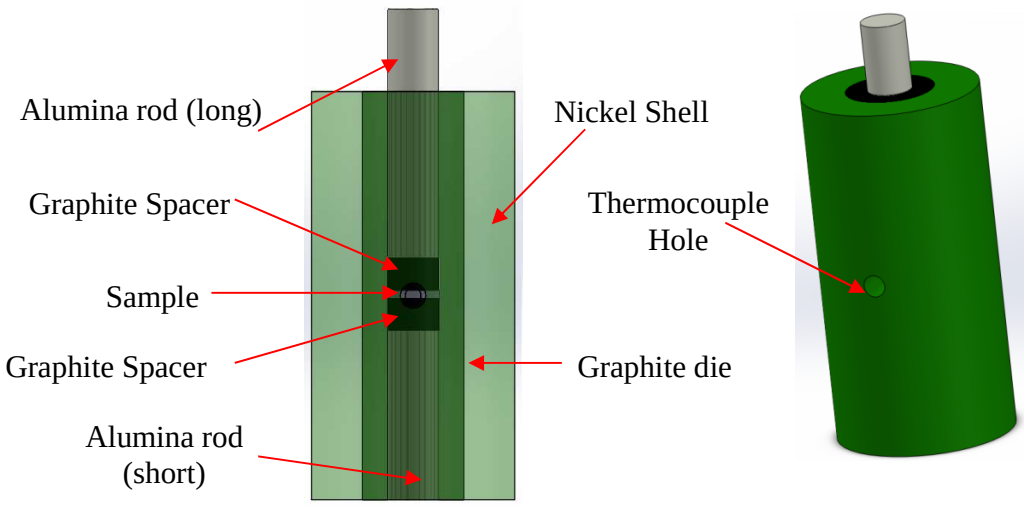


Figure 3.4: Front and isometric CAD drawings of the graphite die assembly.

The die would be placed on the press' lower piston within the induction heating coil, and secured by the upper piston. An insulation layer (alumina silicate) was placed between the die and the lower piston. After heat is applied to the die, the pellet press would then raise the lower piston, to apply pressure to the sample via the long rod. A thermocouple was placed through the nickel shell and on the graphite die to measure the temperature of the die during the procedure.

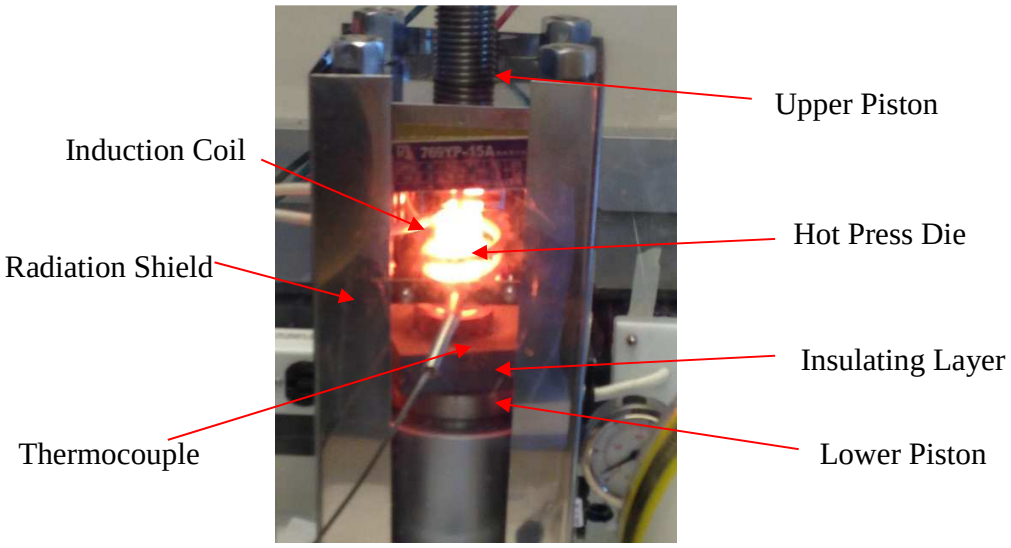


Figure 3.5: Close up photo of hot pressing set-up.

During the hot pressing procedure, the air inside the glove box was continuously vacuumed while argon gas flowed into the glove box. This allowed the procedure to be performed in an atmosphere of 2-5 ppm oxygen, thereby reducing the chance of the sample oxidizing during heating.

3.3 – Sample Preparation

The compacted silicon nanowires sample examined for this thesis was fabricated from vapor-liquid-solid (VLS) nanowires. The nanowires were grown on silicon wafers using gold as a catalyst. The average diameter of the nanowires was 190 nm. The images of the nanowires and the distribution of the nanowire diameters are shown below. About 1.5 wafers were used to grow the silicon nanowires for this sample, from which around 35 mg of nanowires were extracted.

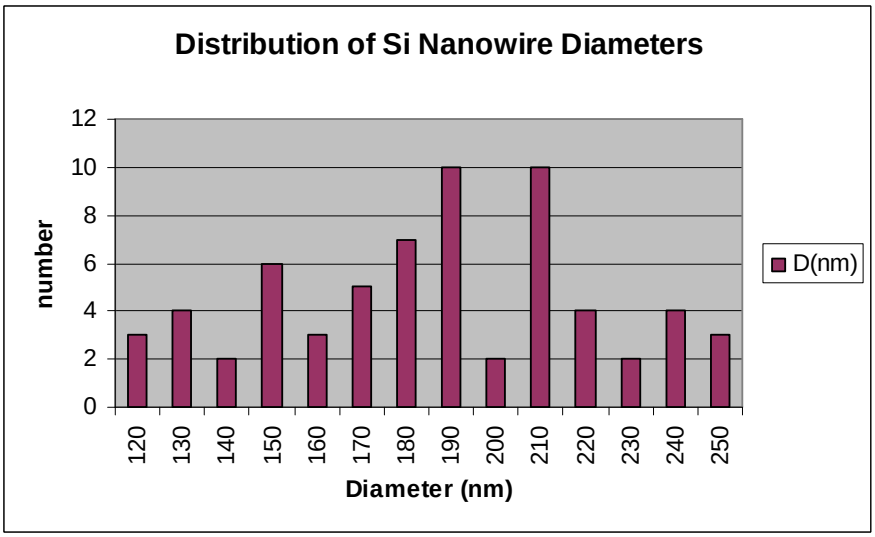


Figure 3.6: Distribution of silicon nanowire diameters.

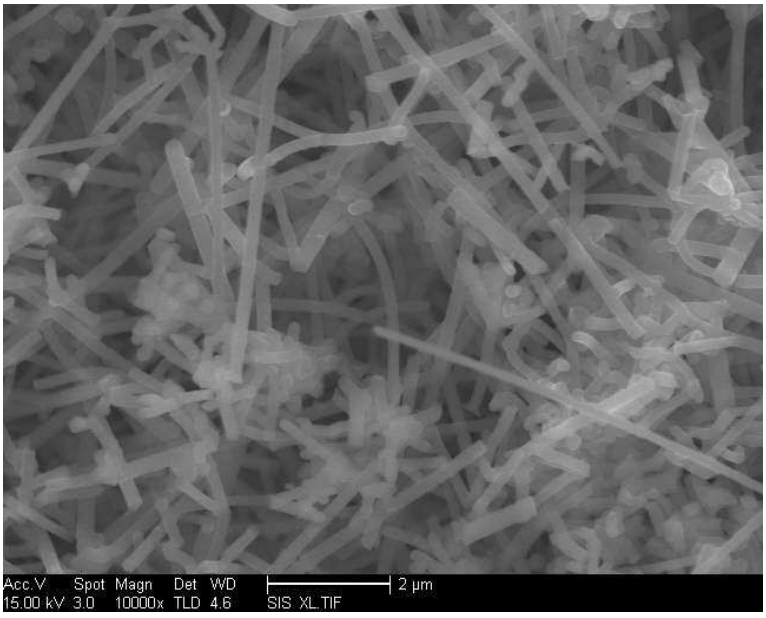


Figure 3.7: SEM image of silicon nanowires

After the nanowires were grown, they were treated in a 20:1 buffered oxide etch (BOE) solution for one minute to remove the oxide layer from the nanowires. The wafers were then rinsed in methanol for at least 10 min to remove the etchant from the wafers. The wafers were rinsed at least 3 times in methanol. Methanol was used instead of DI water to reduce the possibility of the nanowires oxidizing. The nanowires were then removed from the wafers in methanol by scratching the wafer with a razor blade (figure 3.8). The wafers were scratched until a gray surface was seen, indicating a large percentage of the nanowires have been removed. However, the scratching procedure also removed large debris of silicon from the wafers.

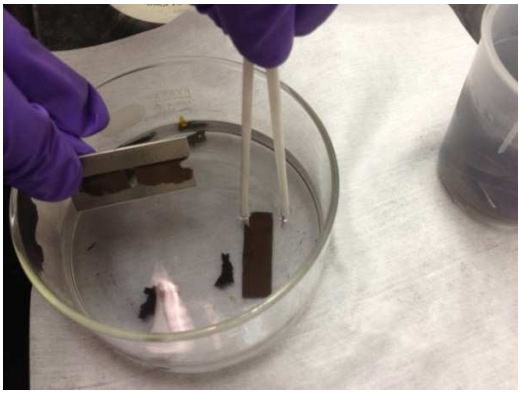


Figure 3.8: Picture of nanowire extraction using a razor blade.

To remove the silicon debris, the methanol-nanowire solution was then poured into an appropriate number of centrifuge vials. Each vial was then sonicated for 2-3 min, after which the solution was poured into a new vial, leaving behind the large silicon debris. This process was repeated at least 3 times.

Afterwards, the methanol-nanowire solution was then centrifuged at 10000 rpm for 5 min and then at 4000 rpm for 30 min. As much of the methanol liquid as possible was removed from the vials, leaving behind dense masses of silicon

nanowires in small amounts of methanol. The procedure was repeated until all the silicon nanowires were condensed into a single vial. The nanowires were then dried overnight in the transfer chamber of the glove box before being placed inside the glove box. The nanowires were hot pressed at 1190 C under 150 MPa of pressure for 40 min.

3.4 – Sample Characteristics

The resulting pellet was measured to be 0.665 mm thick with a mass of 0.0349g. The diameter was estimated to be 6.35 mm (the ID of the graphite die). However, the pellet broke into four pieces before this could be confirmed (figure 3.9). The pellet came out of the procedure with cracks, making it fragile. Using the above measurements, the pellet was estimated to have a density of 1.657 g/cm^3, 71.2% of bulk silicon density.

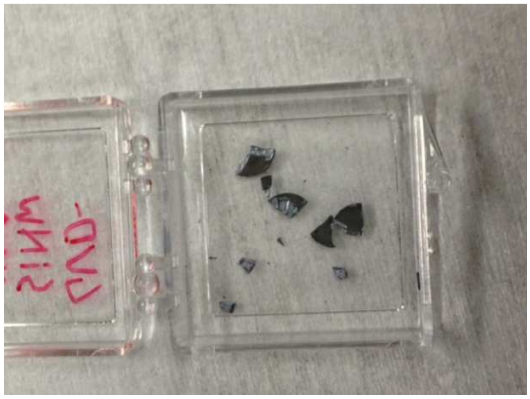


Figure 3.9: Picture of compacted silicon nanowire sample.

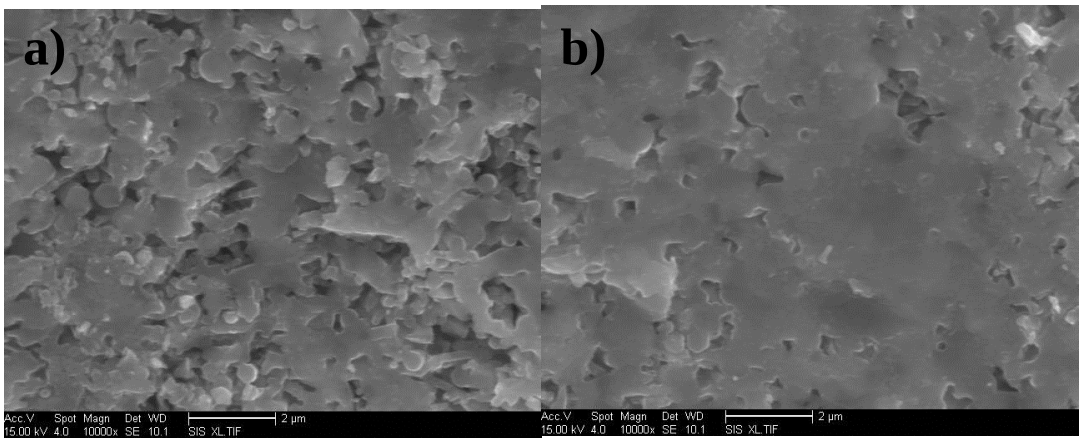


Figure 3.10: SEM images of inside of sample. **a)** Porous section of sample. **b)** More compacted section of sample.

A small piece of the sample was extracted and examined with the SEM to see the silicon nanowire interfaces inside the sample (Figures 3.10). The images show that there are areas where the sample is highly porous and areas where it is more compacted. Nonetheless, it can be seen that hot pressing silicon nanowires have created numerous solid-solid interfaces between nanowires.

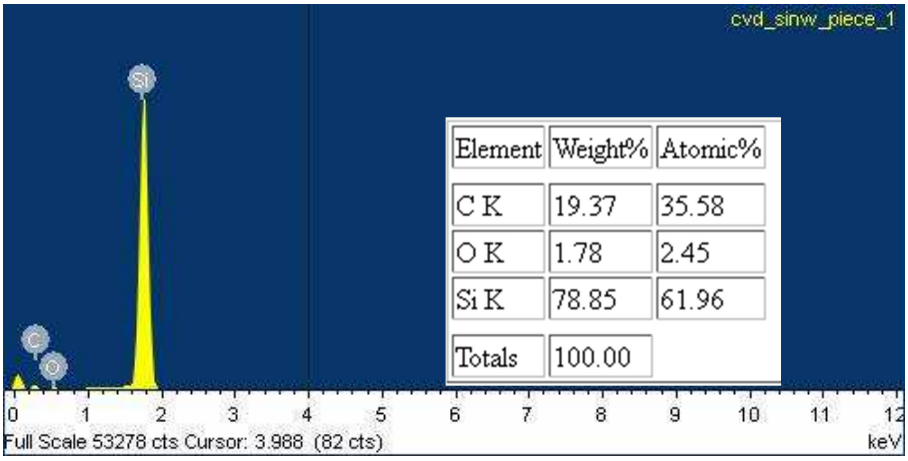


Figure 3.11: EDX composition spectrum of the sample.

To check if the sample has oxide layers inside, the piece was also examined using energy dispersive x-ray spectroscopy (EDX). The EDX analyzed the elemental composition of the inside layer of the sample, the results of which are shown in the figure 3.11. The carbon shown may be due to diffusion of carbon from the graphite spacers into the silicon surface. Since the amount of oxygen present was only ~3 at%, it is safe to say that the inside of the sample was not heavily oxidized. Therefore, the thermal conductivity measured for this sample will be only of the silicon nanowires composite.

To get a clearer picture of the interfaces between the silicon nanowires in the sample, the sample was also examined using Focused Ion Beam (FIB). The image shows the individual nanowires (within red circle) connecting with highly compacted areas of the sample (within yellow circle). These large compacted areas may be the result of some fusion of the nanowires into new crystalline structures. This may change the scattering behavior of the phonons at the interfaces.

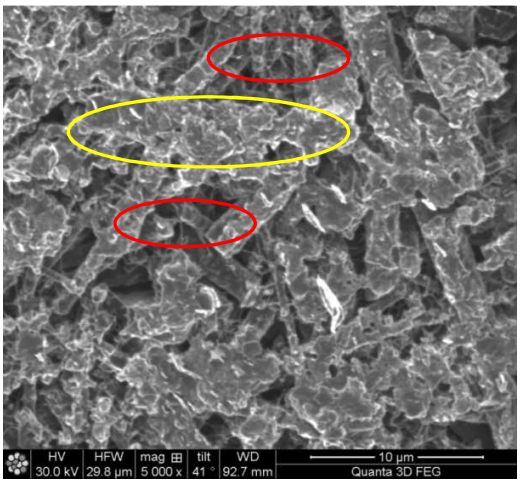


Figure 3.12: FIB image of the sample

Chapter 4: Theoretical Models of Thermal Conductivity of Compacted Silicon Nanowires

4.1 – Introduction to Analytical Modeling for the Thermal Conductivity of Compacted Silicon Nanowires

The thermal conductivity of any material is contributed by the lattice or phonons, k_l, and the electrons, k_e. The total thermal conductivity can therefore be expressed as:

$$k_{total} = k_l + k_e \quad (4.1)$$

In the case of a semiconductor like silicon, the contribution to the thermal conductivity would be dominated by the lattice rather than the electrons. Hence, from this point forward, the thermal conductivity k will refer to the lattice thermal conductivity.

This paper presents an attempt to create a relatively simple analytical model for the thermal conductivity of the compacted silicon nanowire sample. The model consists of two parts: the effective thermal conductivity of the sample due to silicon-silicon interfaces and the effective thermal conductivity of the sample due to porosity effects. The model first calculates the effective thermal conductivity due to thermal boundary resistance at the interfaces, and then considers the porosity effect to calculate the effective thermal conductivity due to the combined effect of thermal boundary resistance and porosity.

4.2 –Effective Thermal Conductivity of Silicon-Silicon Interfaces

The thermal resistance at the interfaces between silicon nanowires can be modeled using the diffuse mismatch model (see Chapter 1). For this analysis, let us assume that the nanowires compacted in the nanocomposite have uniform diameters (d ~ 190 nm) and that the nanowires have a [001] crystal orientation. Since the compacted silicon nanowires only involves interfaces between similar sized silicon nanowires, we can also assume that the acoustic properties of the nanowires are uniform (at the interface between two nanowires, $c_{1,j} = c_{2,j}$). Therefore, we can take the transmission coefficient α to be 0.5 and the transmission probability Γ to be 0.25. After inputting these values into 1.9, the heat conductance at the silicon-silicon interface is:

$$h_{Bd} = \frac{1}{16\pi^2}\frac{\hbar^2}{k_b T^2 c_{1,j}^2}\sum_j \int_0^{\omega_D} \omega^4 \frac{e^{(\frac{\hbar\omega}{k_b T})}}{[e^{(\frac{\hbar\omega}{k_b T})}-1]^2}\, d\omega \qquad (4.2)$$

Knowing that $c_{1,1} = 8.970 \times 10^3$ m/s and $c_{1,2} = c_{1,3}$ 5.332×10^3 m/s, we can calculate h_{Bd} by numerical integration of the integral from 0 Hz to the Debye cut-off frequency ω_D. Afterwards, we can take the reciprocal of h_{Bd} to find the thermal boundary resistance R_{Bd}. The MatLab script used for this calculation is presented in the appendix.

With the calculated R_{Bd}, we can then calculate the effective thermal conductivity of the sample as a result of the interface resistance. There are two popular analytical models used for this calculation: the Nan et al. model[17] and the

Yang et al. model[18]. The Yang et al. model was found to better describe the thermal interfaces between the silicon nanowires and was thus used for the analytical model.

The Yang et al. model begins by examining the temperature profile across a polycrystalline system in response to an applied heat flux.[18] Using the Fourier law, the temperature profile can be modeled as shown in figure 4.1.

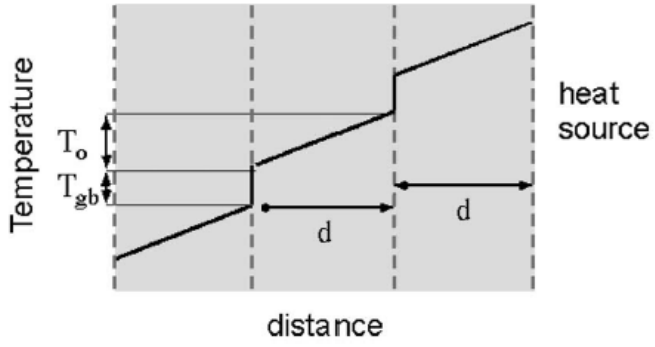


Figure 4.1: Temperature profile across polycrystalline compound with grains of size d.

The temperature difference across a single grain of size d is expressed as:

$$T^* = T_o + T_{gb} \quad (4.3)$$

where T_o is the temperature difference across the interior of the grain and T_{gb} is the temperature difference at the grain boundary. If we take T^*/d to equal dT/dx in Fourier's law, we can define the effective thermal conductivity, k_{eff} of the polycrystalline material as:

$$k_{eff} = \frac{-qd}{T_o + T_{gb}} \quad (4.4)$$

Since $T_o = \frac{-qd}{k_i}$ and $T_{gb} = -qR_{Bd}$, where k_i is the single-crystal thermal conductivity, 4.4 can be rewritten as:

$$k_{eff} = \left[\frac{1}{k_i} + \frac{R_{Bd}}{d}\right]^{-1} \quad (4.5)$$

This expression is valid for samples with d greater than the phonon wavelengths. If d is close to the phonon wavelength, an additional parameter will be needed in equation 4.5. However, for the compacted silicon nanowire sample discussed in this paper, where we take d = 190 nm, equation 4.5 is sufficient.

As stated earlier, another popular model used to calculate k_{eff} is the Nan et al. model. The only difference from the Yang et al. model is the presence of a factor 2 in front of the R_{Bd} term[19]. This might have occurred because the models take two different perspectives of the heat transfer across the grain boundaries (see figure 4.2). Nan et. al model images a single particle surrounded by grain boundaries, such that a heat flux through the particle experiences resistances at two grain boundaries. Yang et. al model accounts for the fact that a grain boundary is shared by two particles, so it is only necessary to account for one grain boundary resistance. Therefore, the Nan et al. model seems to count R_{Bd} twice and is not appropriate for the analytical model.

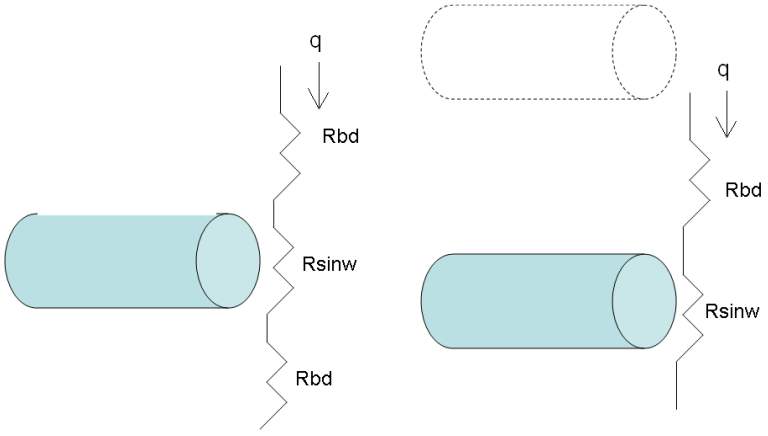


Figure 4.2: Diagram of heat transfer across the silicon nanowire and grain boundaries according to Nan et al. model (left) and Yang et al. model (right).

4.3 - Effective Thermal Conductivity of Porous Medium

Proper modeling heat transfer in a porous medium has been a subject of debate for many decades. The problem of heat transfer in a porous medium was first addressed by Maxwell[20,21,22]. He addressed the problem using the effective medium approximation. According to this approximation, the pores are assumed to be spherical bodies uniformly distributed within a continuous medium of uniform thermal conductivity, k_o. Each pore is said to cause a temperature perturbation at its location, resulting in a change in the conductivity of the medium. The resulting conductivity is known as the effective conductivity of the medium, k_m. Maxwell further assumed that the spacing between the pores sufficiently far enough away from each other such that temperature perturbations caused by one pore does not affect the temperature perturbations caused by other pores. In other words, the pores do not interact with each other. The Maxwell model for a medium with spherical pores is:

$$\frac{k_m}{k_o} = 1 - \frac{3}{2}P \tag{4.6}$$

where P is the porosity of the medium.

The assumption that the pores do not interact with each other is said to be plausible only in mediums with vary dilute pore distributions ($P < 0.1$). Therefore, the Maxwell model is limited only to porous mediums with very specific conditions. An attempt was made by Bruggeman to model heat transfer in porous mediums that have higher porosity and randomly distributed pores. He assumed that the sphere radius of the pores varied within an infinite range of values and the each single sphere was embedded within the continuous matrix. In essence he extended the dilute dispersion

assumption made by Maxwell to cover all pore dispersions (0 < P < 1). The model he derived for spherical pores is:

$$\frac{k_m}{k_o} = (1 - P)^{\frac{3}{2}} \quad (4.7)$$

However, the Bruggeman model, like the Maxwell model, does not consider the effects of pore interactions, which has proven to be more significant for mediums with higher porosity. The pore interaction effects have been considered by D.J. Jeffery when he derived a second order term in the Maxwell model 100 years after the derivation of the Maxwell equation[34]. Pore interaction effects have also been examined by R.E. Meredith and C.W. Tobias. The model they derived, known as the Meredith-Tobias model, has been used to model the thermal conductivity of mediums with randomly oriented spheroidal pores[22]. The model is expressed as:

$$\frac{k_m}{k_o} = \frac{(2-P)}{2+(W-1)P}\frac{2(1-P)}{2(1-P)+WP} \quad (4.8)$$

where $W = \frac{1}{3}(\frac{1}{2F} + \frac{2}{1-F})$ and F is the shape factor of the pores. For spherical pores, F = 1/3, meaning that equation 4.8 becomes:

$$\frac{k_m}{k_o} = \frac{(2-P)(1-P)}{(2-0.125P^2)} \quad (4.9)$$

The compacted silicon nanowire composite is viewed as a continuous medium filled with spherical pores. Since the porosity of the sample is estimated to be around 0.288, the Maxwell model would not be an appropriate model. The Meredith-Tobias model is the preferred model because it considers pore interactions.

4.4 – The Analytical Model of the Thermal Conductivity of Compacted Silicon Nanowires

The analytical model estimates the thermal conductivity of the compacted silicon nanowires by considering both the thermal boundary resistance effects and the porosity effect. The Yang et al. model (4.5) was used to calculate the effective thermal conductivity k_{eff} of the nanowires due to the thermal boundary resistance at the interfaces of the nanowires. This was calculated by entering the temperature dependent thermal conductivity for a single crystal 190 nm diameter nanowire as k_i in 4.5. However, since actual experimental k for a 190 nm nanowire was not available, k_i was extrapolated from experimental k of 37 nm, 56 nm, and 115 nm nanowires. By examining the differences between the k of these nanowires, a factor was derived based on temperature and diameter, and used to extrapolate k for 190 nm nanowires. The temperature T used in the model ranged from 30 K to 320 K. As said before, the grain size d was assumed to be the same as the diameter of the nanowires (d = 190 nm).

k_{eff} is now considered to be the thermal conductivity of the sample medium. After k_{eff} is calculated, it is entered into the Meredith-Tobias model (4.9) as k_o. The porosity P was calculated using the density of the sample and bulk silicon, $P = 1 - \frac{\rho_{sample}}{\rho_{bulk\ Si}}$, which was calculated to be 0.288. In summary, the expression of the analytical model is:

$$k_m = \frac{(2-P)(1-P)}{(2-0.125P^2)} \left[\frac{1}{k_i} + \frac{R_{Bd}}{d}\right]^{-1} \qquad (4.10)$$

4.5 – Monte Carlo Simulation of Phonon Tranport in Compacted Silicon Nanowires

A theoretical study of compacted silicon nanowires thermal conductivity had already been performed by Weixue Tian and Ronggui Yang. They used a Monte Carlo simulation to study phonon transport within the silicon nanowire composite[24]. First, they simplified the structure of the composite into a chess board-like structure as shown in the figure below. The structure can then be broken down into two types of unit cells as shown below. Each square in the unit cell represents a different phase of material in the composite structure. The model structure was originally designed to study phonon transport in a compacted composite consisting of Si and Ge nanowires, but Tian and Yang also performed a comparative study on compacted composites containing only silicon nanowires. They probably used a unit cell similar to the ones shown in the figure below, replacing the Ge phases with Si phases. As can be seen in the figure, the nanowires are assumed to be perfectly aligned, with no pores in the medium.

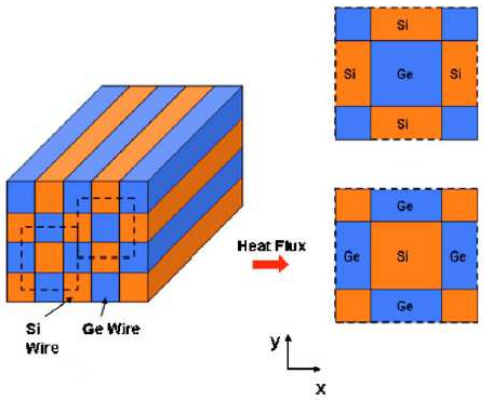


Figure 4.3: Theoretical structure and unit cells of compacted nanowire composites used in Monte Carlo Simulation.[24]

Second, within each square of the unit cell, they averaged the properties of the phonons at equilibrium and assigned them into phonon energy bundles. The phonon energy bundles are assumed to drift in the nanocomposites with average velocity (v_{avg}) and average frequency, both of which were estimated by averaging the equilibrium phonon dispersion curves of the three acoustic phonon branches. Thus, the phonons in each energy bundle at the initiation of the simulation were assumed to exist at the same frequency and group velocity, corresponding to the gray media approximation[24]. Only the mean free paths of the phonons were temperature dependent, which were estimated using experimental bulk thermal conductivity. These temperature dependent properties were pre-calculated and stored into the computer memory before the simulation began.

The basic principle of the Monte Carlo Simulation used by Tian and Yang is to track down the phonon energy bundles as they drift and collide through the computation domain or unit cell. The domain was typically divided into 24 x 24 subcells each containing 10,000 phonons which were assigned to an energy bundle. The phonon energy bundles underwent "intrinsic" and interface scattering as they passed through the nanocomposite. Intrinsic scattering mechanisms included isotropic scattering (most likely meaning phonon-phonon scattering), defect scattering, and electron phonon scattering. The intrinsic scattering effects were lumped together through approximate mean free path estimated from experimental thermal conductivity k_{bulk} and heat capacity C_{ac} of bulk silicon. The following equation was used to calculate the mean free paths at different temperatures:

$$\Lambda(\mathrm{T}) = \frac{3\,k_{bulk}(T)}{v_{avg}C_{ac}(T)} \tag{4.11}$$

The estimated mean free paths were then used to calculate the scattering probability of the phonons using the following equation:

$$P_s = 1 - e^{-\frac{v_{avg}\Delta t}{\Lambda(\mathrm{T})}} \tag{4.12}$$

The assumption made in equation 4.12 was that the "intrinsic" scattering events happens similarly in bulk materials as that in nanocomposites.[25] At the end of each time step, Δt, each phonon was treated for phonon-intrinsic scattering, during which P_s was calculated and a random number between 0 and 1 was drawn. The random number was than compared to P_s. If the number was less than P_s, the phonon was considered scattered. If scattered, two more random numbers, R_1 and R_2 (both between 0 to 1), were selected to determine the scattering direction using:

$$s_i = \sin(\theta)\cos(\Psi)\,\hat{\imath} + \sin(\theta)\sin(\Psi)\,\hat{\jmath} + \cos(\theta)\,\hat{k} \tag{4.13}$$

where $\cos(\theta) = 2R_1 - 1$ and $\Psi = 2\pi R_2$. θ is the angle between the vector s_i and direction k (range: 0 to π), and Ψ is the angle between the vector s_i and the direction i (range: 0 to 2π). For interface scattering, the interface was assumed to be diffuse[24,25]. The coefficient of transmission, $\alpha_{1\text{-}2}$ (ω), at a diffusive interface is given by equation 1.11 according to the diffusive mismatch model.

$$\alpha_{1\to2}(\omega) = \frac{\sum_j c_{2,j}N_{2,j}(\omega,T)}{\sum_j c_{1,j}N_{1,j}(\omega,T)+\sum_j c_{2,j}N_{2,j}(\omega,T)} \tag{1.11}$$

$\alpha_{1\to2}(\omega)$ was estimated based on the average phonon group velocity and energy density at both sides of the interface, simplifying equation 1.11 to:

$$\alpha_{1\to2} = \frac{v_{avg,2}N_2(T)}{v_{avg,1}N_1(T)+v_{avg,2}N_2(T)} \quad (4.14)$$

Here $\alpha_{1\to2}$ is not frequency dependent. The interface scattering event was considered when a phonon hits an interface, during which a random number (between 0 and 1) was drawn and $\alpha_{1\to2}$ is calculated[25]. If the random number was larger than $\alpha_{1\text{-}2}$, the phonon was transmitted. Otherwise, the phonon was reflected. At this point, two more random numbers were chosen, R_1 and R_2, and inputted into the following expression to calculate the transmission or reflection direction.

$$s_r = \sin(\theta)\cos(\Psi)\,\hat{t_1} + \sin(\theta)\sin(\Psi)\,\hat{t_2} + \cos(\theta)\,\hat{n} \quad (4.15)$$

where $\sin^2(\theta) = R_1$ and $\Psi = 2\pi R_2$. $\hat{t_1}$ and $\hat{t_2}$ represent the directions tangent to the interface plane, while $\hat{n}$ is the direction normal to the interface plane. Similar to the intrinsic scattering expression, θ is the angle between the vector s_r and direction n (range: 0 to $\frac{\pi}{2}$ for reflection and 0 to -$\frac{\pi}{2}$ for transmittance), and Ψ is the angle between the vector s_r and the direction t_1 (range: 0 to 2π). Diagrams of the scattering events are shown below.

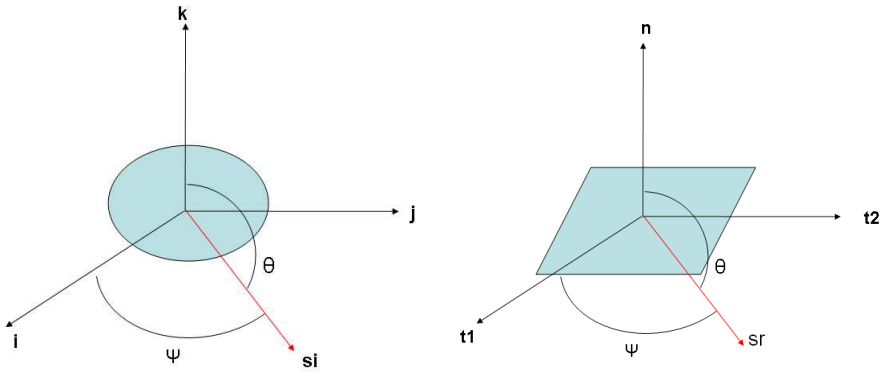


Figure 4.4: Diagrams of intrinsic scattering event (left figure) and interfacial scattering event (right figure) used for Monte Carlo Simulation

The Monte Carlo Simulation began by setting up a unit cell as shown in figure 4.6 with boundary conditions at y = 0, y = L_y (size of unit cell in y direction), x = 0 and x = L_x (size of unit cell in x direction). The boundary conditions at y = 0 and y = L_y were set to be periodic, such that for each phonon leaving a cell boundary, another phonon with exactly the same properties (direction, position, and velocity) enters the cell from the opposite boundary. The boundary conditions at x = 0 and x = L_x were also set to be periodic. A heat flux q was applied to the unit cell such that q(0 , y) = q(L_x , y). This generated a temperature gradient from x = 0 to x = L_x.

After the boundary conditions were set, the simulation then tracked down phonons leaving the boundaries. Whenever a phonon encountered a scattering event, that phonon was said to have been deleted and replaced with a new phonon (with new direction, position, and velocity based on local conditions at the scattering event). The new phonon then continued to move in a new direction randomly chosen by the scattering events (eq. 4.23 and 4.25) until it encounters another scattering event. Each phonon was tracked down with a certain time step, Δt. At the end of each Δt, the energy of the phonons were recorded. Any difference in energy that occurred at a scattering event within a subcell of the unit cell was noted in order to display a temperature distribution across the unit cell (figure 4.8a). From the distribution, temperature gradients can then be calculated across the unit cell, which can be used to calculate the thermal conductivity of the unit cell. Although this explanation mainly covered 2-D heat transfer within compacted nanocomposite, the simulation can also be expanded to analyze 3-D heat transfer.

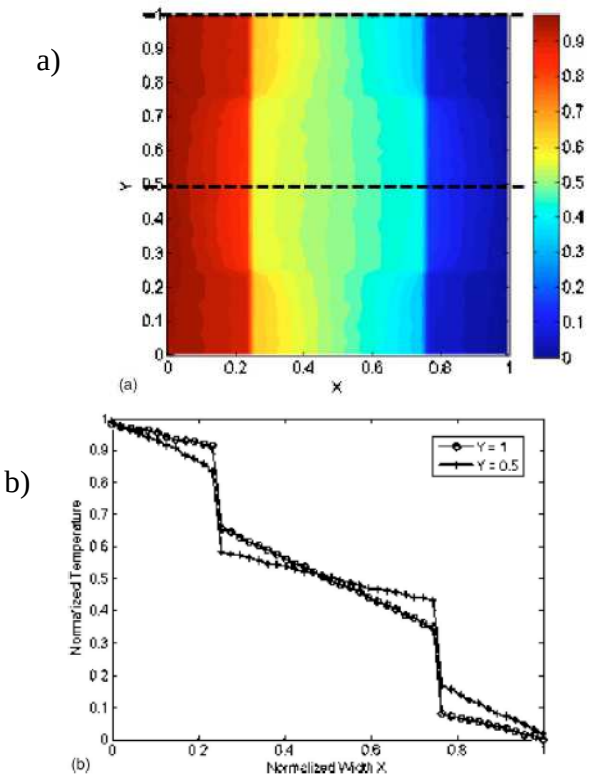


Figure 4.5: a) Normalized temperature distribution in a unit cell of compacted nanocomposite. b) Temperature at Y = 0.5 and Y = 1 indicated by the two dashed lines in (a)

Chapter 5: Measurement of Thermal Conductivity of Compacted Silicon Nanowires

5.1 – The 3ω Method

One of the most widely accepted methods for measuring the thermal conductivity of materials is the 3ω method. The 3ω method is a frequency domain thermal conductance method developed by Cahill[26,27]. The method was designed to measure the thermal conductance of thin film samples. The schematic setup of the sample is shown below.

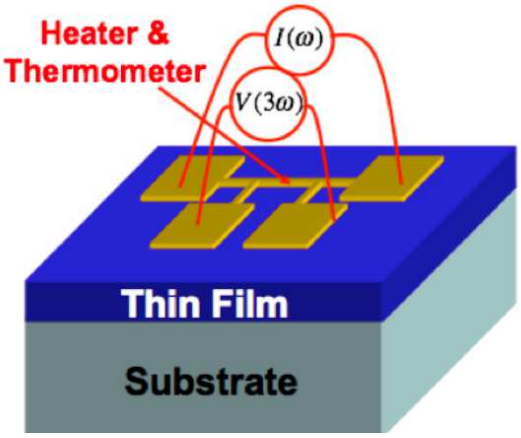


Figure 5.1: Schematic arrangement of the sample for 3ω method.[26]

The thin film sample is bonded to a dielectric substrate (usually silicon) using an epoxy. A micropattern four-point metal film heater (usually gold) is deposited on the sample, where an AC current is applied along the narrow metal line of the heater as shown in Figure 5.1. Voltage readings are taken at the two points connected to the heater. The AC current source supplies a sinusoidal current with frequency ω, which can be expressed as:

$$I = I_o \sin(\omega t) \qquad (5.1)$$

where I_o is the amplitude of the AC current. The current produces joule heating in the heater expressed as:

$$q = I^2R = I_o^2 sin^2(\omega t)R_{so} \quad (5.2)$$

where R_{so} is the sample resistance without considering temperature effects. The expression above can then be simplified as:

$$q = \frac{I_o^2 R_{so}}{2} - \frac{I_o^2 R_{so}}{2}\cos(2\omega t)$$

$$q = q_{DC} + q_{2\omega}\cos(2\omega t) \quad (5.3)$$

The current generates both DC heat and heat at 2ω frequency. This means that the temperature of the sample also fluctuates at 2ω with an amplitude of $\Delta T_{2\omega}$. The temperature is typically out of phase of the generated heat by φ. The temperature fluctuation causes a small change in the resistance felt by the sample, which is described by the temperature coefficient of resistance (TCR). The resistance of the sample is thus expressed as:

$$R_s = R_{so} + (\frac{dR}{dT})\Delta T_{2\omega}\cos(2\omega t + \varphi) \quad (5.4)$$

The voltage drop across the heater is then expressed as:

$$V = IR_s = I_o R_{so}\sin(\omega t) + I_o\left(\frac{dR}{dT}\right)\Delta T_{2\omega}\cos(2\omega t + \varphi)\sin(\omega t)$$

$$V = V_o\sin(\omega t) + \left(\frac{V_o}{R_{so}}\right)\left(\frac{dR}{dT}\right)\left(\frac{\Delta T_{2\omega}}{2}\right)[\sin(3\omega t + \varphi) - \sin(\omega t + \varphi)]$$

$$V = \left[V_o\sin(\omega t) - \left(\frac{V_o}{R_{so}}\right)\left(\frac{dR}{dT}\right)\left(\frac{\Delta T_{2\omega}}{2}\right)\sin(\omega t + \varphi)\right] +$$

$$\left[\left(\frac{V_o}{R_{so}}\right)\left(\frac{dR}{dT}\right)\left(\frac{\Delta T_{2\omega}}{2}\right)\sin(3\omega t + \varphi)\right]$$

$$V = V_{1\omega}\sin(\omega t + x) + V_{3\omega}\sin(3\omega t + \varphi) \quad (5.5)$$

Measurements of the voltage drop across the heater include both $V_{1\omega}$ and $V_{3\omega}$. However, by connecting a lock-in amplifier along with a potentiometer to the 3ω circuit, the $V_{1\omega}$ reading can be cancelled out to extract the desired $V_{3\omega}$ reading. A schematic of the circuit is shown below.

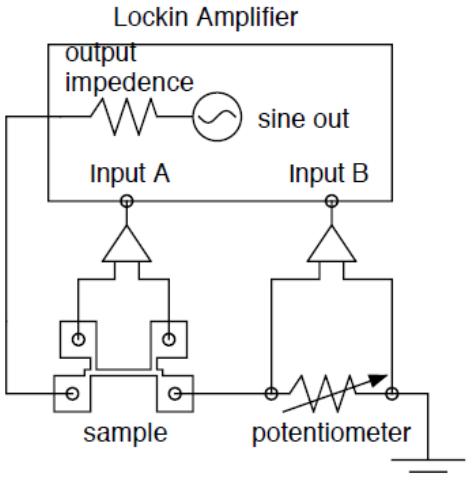


Figure 5.2: Schematic of 3ω circuit.[26]

By rearranging the $V_{3\omega}$ component in equation 5.5, $\Delta T_{2\omega}$ can then be related to $V_{3\omega}$ as:

$$\Delta T_{2\omega} = 2\left(\frac{dT}{dR}\right)R_{so}\left(\frac{V_{3\omega}}{V_o}\right)$$

$$\Delta T_{2\omega} = 2(TCR)^{-1}\left(\frac{V_{3\omega}}{V_o}\right) \qquad (5.6)$$

In most experimental setups, the temperature fluctuation is so small such that $V_o \sim V_{1\omega}$. The transient heat equation for this setup with a heater of L length and 2b width is given as:

$$\Delta T_{2\omega} = \frac{p}{L\pi k_s}\int_0^\infty \frac{sin^2(Kb)}{[K^2b^2(K^2+\delta^2)^{\frac{1}{2}}]}dK$$

$$\delta^2 = \frac{2i\omega\rho C}{k_s} \qquad (5.7)$$

where p is the heater power, K is the wave vector, C is the sample specific heat, ρ is the sample density, and k_s is the sample thermal conductivity. δ is known as the thermal penetration depth. According to Cahill, if the heater is thin compared to the sample such that $\ll \frac{1}{b}$, equation 5.7 can simplify to[27]:

$$\Delta T_{2\omega} = \frac{p}{L\pi k_s}\left[0.5\ln\left(\frac{k_s}{\rho C b^2}\right) - 0.5\ln(2\omega) + \eta - i\left(\frac{\pi}{4}\right)\right] \quad (5.8)$$

By taking the derivative of $\Delta T_{2\omega}$ with respect to ln(2ω), the thermal conductivity of the sample can be evaluated by:

$$k_s = \frac{-p}{2\pi L}\frac{d(\ln(2\omega))}{d(\Delta T_{2\omega})} \quad (5.9)$$

Using equation 5.9, the thermal conductivity of the sample can be evaluated based on the slope of ln(2ω) with respect to $\Delta T_{2\omega}$. This is known as the "slope method". By combining equation 5.6 with 5.9, k_s can be evaluated based on the slope of ln(2ω) with respect to $V_{3\omega}$ as shown in the following equation:

$$k_s = \frac{-p(TCR)V_{1\omega}}{4\pi L}\frac{d(\ln(2\omega))}{d(V_{3\omega})} \quad (5.10)$$

The slope method is useful to quickly calculate the thermal conductivity of the sample from the frequency and $V_{3\omega}$ data collected by through the 3ω method. The method is valid if $V_{3\omega}$ is linearly dependent on ln(2ω). However, this was not the case when measuring the compacted silicon nanowire sample. It was more appropriate to use equation 5.7, which can be evaluated using a numerical analysis program such as MatLab. This method will be explained in more detail later.

5.2 – Sample Set-up

A piece of the compacted silicon nanowires pellet was selected for the thermal conductivity measurement. Because of the brittleness of the sample, the piece was first placed into an epoxy mold to provide support for the sample. After curing for at least 24 hours, the epoxy mold was polished until a smooth flat sample surface was exposed on one side.

PMMA was then spin-coated onto the sample surface in order to form a dielectric layer between the sample and the heater. Afterwards, the gold heater was deposited onto the PMMA layer using plasma sputtering deposition. The four point heater was formed by placing a shadow mask template unto the sample when sputtering gold. The sample was then bonded to a silicon chip as shown below.

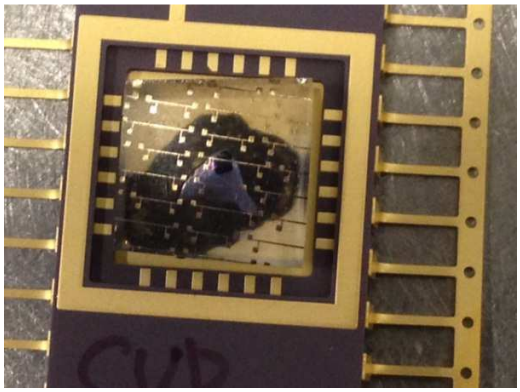


Figure 5.3: Sample with heater.

Gold wires were then bonded to the heater and chip assembly using silver epoxy in order make the electronic connections needed to apply current to the heater and to measure the voltage drop across the heater. The bonded wires are shown in the picture below.

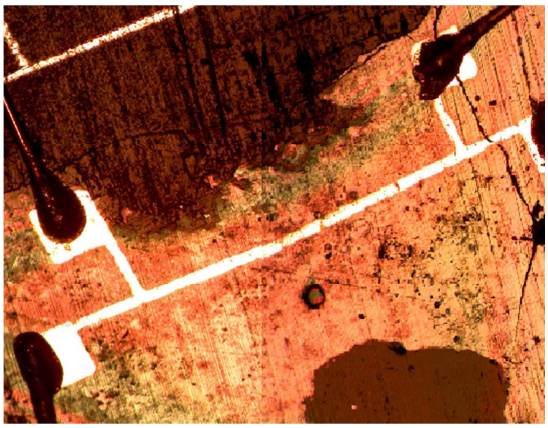


Figure 5.4: Gold wire bonded to heater

The sample was then connected to the 3ω circuit and placed into a vacuum chamber. The 3ω voltages were measured for current frequencies from 5 to 2000 hz at temperatures from 300 K to 40 K. Liquid nitrogen was flowed into the chamber in order to lower the chamber temperature down to 40 K. The power input into the heater, the sample resistance, 1ω DC voltage, and the temperature of the sample were also measured at each temperature. The voltage data was then converted to temperature rise $\Delta T_{2\omega}$ using the calculated TCR and the measured 1ω DC voltages through equation 5.6.

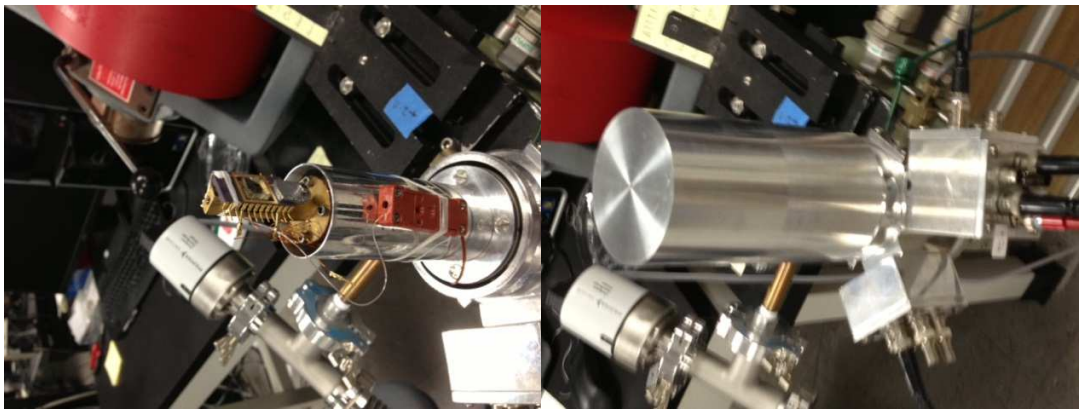


Figure 5.5: 3ω measurement setup before (left) and after (right) closing the vacuum chamber

5.3- Results and Discussion

The thermal conductivity of the compacted silicon nanowire sample was calculated for temperatures between 60 K and 300 K. Because the heater broke at 40K, no useful data was collected at this temperature. The thermal conductivity was calculated from the data by a curve fitting method using MatLab. The sample had a finite thickness and was composed of multiple layers, making the slope method inappropriate for this calculation.

The compacted Si nanowire composite sample, the sample has a layer of PMMA on the Si nanowire composite layer and an epoxy mold layer under the Si nanowire layer. The thermal conductivity of the Si nanowire layer would definitely be higher than those of PMMA or the epoxy layers, but the presence of the PMMA and epoxy layer may affect the heat transfer through the sample. A more generalized formula of equation 5.7 had been developed by Borca-Tasciuc, et. al, to describe 2-D heat conduction across a multilayer-film-on-substrate system[28]. This formula was numerically integrated by MatLab to calculate temperature rise (ΔT) for each frequency (ω):

$$\langle \Delta T \rangle = \frac{-p}{\pi L k_{y1}} \int_0^\infty \frac{1}{A_1 B_1} \frac{\sin^2(b\lambda)}{b^2 \lambda^2} d\lambda$$

$$A_{i-1} = \frac{A_i \dfrac{k_{y,i} B_i}{k_{y,i-1} B_{i-1}} - \tanh(\phi_{i-1})}{1 - A_i \dfrac{k_{y,i} B_i}{k_{y,i-1} B_{i-1}} \tanh(\phi_{i-1})}, i = N..2$$

$$B_i = \left(\eta_i \lambda^2 + \frac{i2\omega}{\alpha_{y,i}} \right)^{1/2}, \quad \phi_i = B_i d_i, \quad \eta = k_x / k_y \tag{5.11}$$

where i is the layer number (with 1 being the top layer and N being the bottom layer), p is the power input, L is the heater length, b is half the heater width, α is the thermal diffusivity, and d is the layer thickness. (note: only here is the wave vector (K) labeled as λ) . The ratio of the in-plane and cross-plane thermal conductivities (η) is close to 1, as previous experimental work has shown[2, 27,28]. *B* is equivalent to $(K^2 + q^2)^{1/2}$ in equation 5.7. *A* is a multiplying factor that considers the effects of heat transfer through layers of different material. When i = N, A_N depends on the boundary condition of the bottom surface of the sample. For the compacted Si nanowire composite sample measured, the bottom surface was considered isothermal, such that $A_N = \frac{-1}{\tanh(B_N d_N)}$.

The curve fitting method was initialized using literature values of k, C, ρ, for PMMA, the Epoxy, and silicon, as well as measured values for b, d, L, and p. From the initial boundary condition A_N, A and B were calculated for each layer until the A_1 and B_1 were calculated. Afterwards, the ΔT was calculated for each ω, and then plotted with respect to ω. The experimental data for ΔT were also plotted with respect to ω and compared to the calculated values (figure 5.6). The calculated curve

was then fitted onto the experimental curve by adjusting the values of k for PMMA and silicon (figure 5.7). After fitting the curve, the k for silicon was then recorded.

```
33 —    dSiNW=.6e-3;
34 —    dMold = 0.1e-9;
35 —    dPMMA= 1.5e-6;
36
37
38 —    d3=dMold;
39 —    d2=dSiNW;
40 —    d1=dPMMA;
41
42
43 —    kMold=.2;
44 —    kSiNW = 30;
45 —    kPMMA=.16;
46
47 —    k3=kMold;
48 —    k2=kSiNW;
49 —    k1=kPMMA;
50 —    k3xy = 1;
```

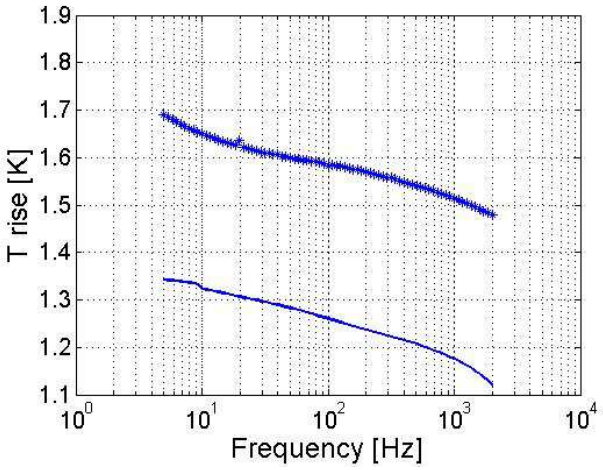


Figure 5.6: Initial output of the curve fitting method

```
35 —    dPMMA= 1.5e-6;
36
37
38 —    d3=dMold;
39 —    d2=dSiNW;
40 —    d1=dPMMA;
41
42
43 —    kMold=.2;
44 —    kSiNW = 44;
45 —    kPMMA=.12;
46
47 —    k3=kMold;
48 —    k2=kSiNW;
49 —    k1=kPMMA;
50 —    k3xy = 1;
```

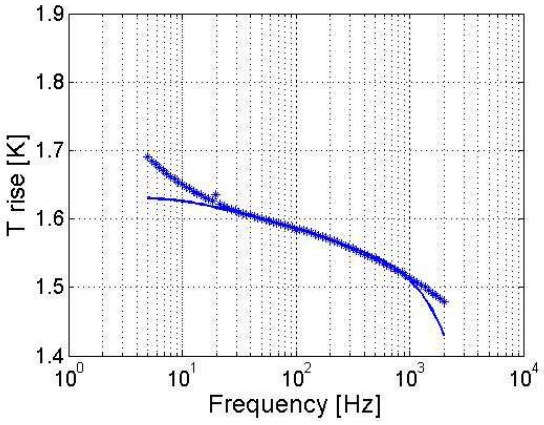


Figure 5.7: Output of the curve fitting method after adjusting thermal conductivity of Si Nanowire and PMMA

The experimental thermal conductivity of the compacted Si nanowire sample is shown below. It is compared to the data of the 190 nm and 115 nm silicon nanowire.

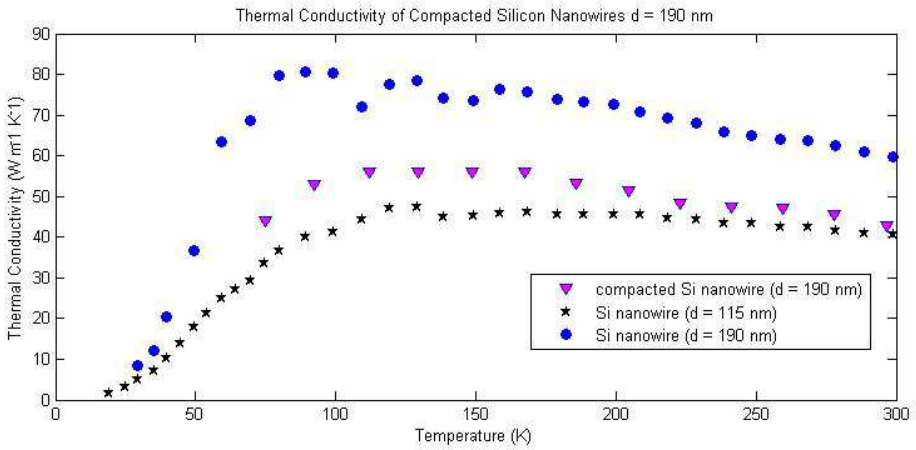


Figure 5.8: Thermal conductivity of compacted silicon nanowires and single crystal nanowires.

Figure 5.8 clearly shows that the composite sample's thermal conductivity is lower than the thermal conductivity of the 190 nm silicon nanowire by almost a factor of 2. The reduction in thermal conductivity can be attributed to diffusive scattering at the interfaces between the silicon nanowires as well as boundary scattering within the individual nanowires. One interesting note to make is that the thermal conductivity of the compacted silicon nanowire sample follows a similar trend to that of smooth single crystal nanowires with d = 115 nm (figure 5.11). Despite the fact that the sample was created from nanowires with diameters that were nearly two times larger, the thermal conductivity of the compacted sample is similar to that of a 115 nm nanowire. This suggests that scattering within the compacted silicon nanowire sample results in a thermal conductivity similar to that of a single crystal nanowire of a smaller diameter.

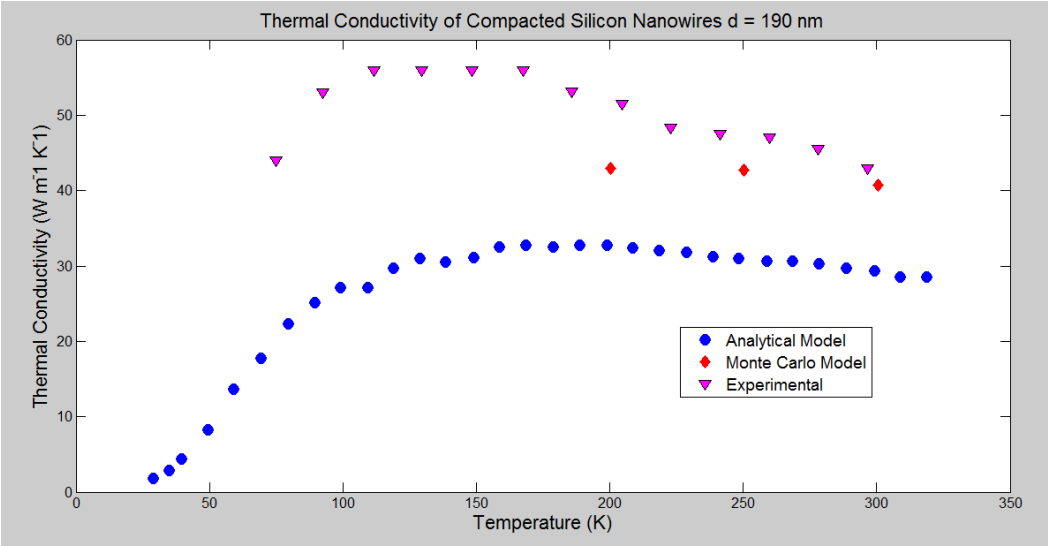


Figure 5.9: Experimental thermal conductivity of compacted silicon nanowires compared to Monte Carlo model and analytical model.

The comparison between the experimental thermal conductivity of the compacted silicon nanowire sample and the Monte Carlo and analytical models is shown in Figure 5.9. The experimental values of k from 200 K to 300 K seem to be close to the values predicted by the Monte Carlo simulation performed by Tian and Yang[24]. The experimental values also seem to follow the same trend as that predicted by the Monte Carlo Simulation for this temperature range. The Monte Carlo simulation assumed that the scattering events within the nanocomposite sample would be very similar to those observed in bulk silicon, and used gray media approximation and bulk silicon thermal conductivity and heat capacity values to initiate the simulation. So far, this method seems to have been appropriate to predict the thermal conductivity of sample for high temperatures. There is insufficient data to say if the

Monte Carlo simulation will hold for lower temperatures. It should be noted that Monte Carlo simulation did not consider porosity effects, which brings some curious questions about the structure of the compacted silicon nanowire sample.

The values predicted by the analytical model, however, are noticeably lower than the experimental values. The analytical model assumed diffusive interface scattering at all nanowire interfaces as well as spherical pores uniformly dispersed within the sample. A plot comparing the analytical model with P = 0 (assuming no porosity) with the experimental values is shown below.

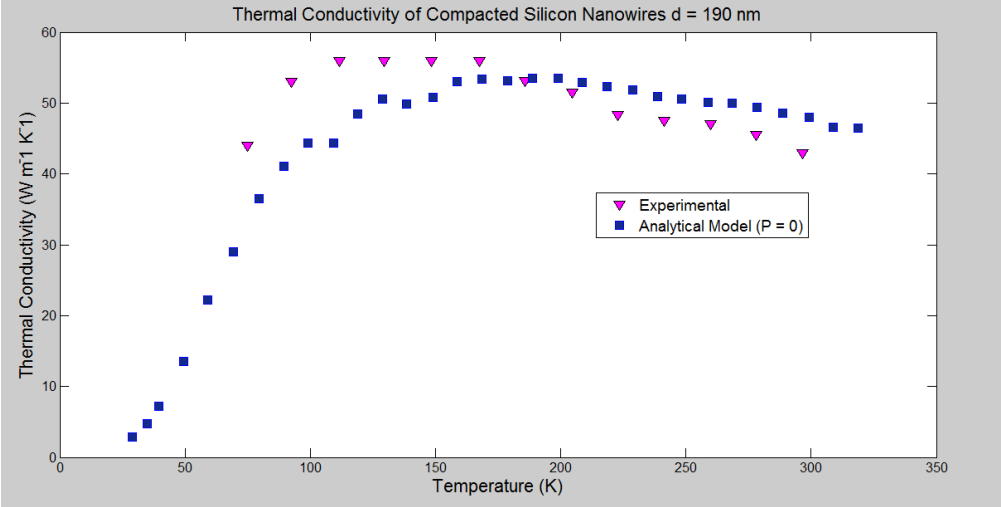


Figure 5.10: Comparison of thermal conductivity of compacted Si nanowire composite with analytical model (where P = 0).

When P = 0, the analytical model considers only the thermal boundary resistance effect at the silicon nanowire interfaces, as descried by Yang et al. model. Figure 5.11 shows that when considering only the thermal boundary resistance effects, the analytical model follows a similar trend to the experimental values for higher

temperatures (T > 200 K in the figure). When the analytical model considers the porosity effect, it assumes that the sample is a continuous medium with insulating spherical inclusions. We can infer from the experimental results that this may not be an accurate view of the sample's structure. A more detailed analysis on the structure of the compacted silicon nanowire sample would be needed to make a more accurate model.

However, as shown in figure 5.11, the analytical model does not follow the thermal conductivity of compacted silicon nanowire composites for lower temperatures (T < 200 K in the figure). This result is somewhat counter-intuitive, since phonons in a sample have longer mean free paths at lower temperatures, it is expected that more phonons would be scattered at the interfaces of the nanowires.

One explanation for this discrepancy is that the analytical model did not consider the frequency dependence of mean free paths. According to thermal conductivity measurements of nanocrystalline silicon performed by Wang, et al., the frequency dependence of the mean free paths becomes important at lower temperatures.[29] These measurements have shown that the mean free paths for grain boundary scattering have ω^{-1} frequency dependence. This has been used to explain the appearance of a k proportion to T^2 trend observed at low temperatures, instead of the expected T^3 trend. This would decrease the thermal resistance at the interfaces, leading to higher thermal conductivity values. The experimental results may infer a similar effect occurred in this compacted nanowire sample.

Chapter 6: Conclusions and Future Works

This research has experimentally demonstrated the reduced thermal conductivity of compacted silicon nanowires that have been predicted by previous theoretical models. The reduction in thermal conductivity can be attributed to diffusive scattering at the interfaces between the silicon nanowires as well as boundary scattering within the individual nanowires. The diffusive mismatch model seems to have been an appropriate starting point to describe the thermal resistance at the interfaces of the silicon nanowires, as indicated by the Monte Carlo simulation performed by Tian and Yang[24]. The result of the Yang et. al model also suggests that diffusive scattering occurs at the interfaces.

A simple analytical model that combined a thermal boundary resistance model with a porous medium model has not been accurate in describing the heat transfer within the compacted silicon nanowire composite. A more detailed analysis on the compacted silicon nanowire structure is needed to find an appropriate model. The Yang et. al model proved effective at predicting thermal conductivity values for high temperatures . However, the model cannot accurately account for the thermal conductivity of the composite material for low temperatures. The experimental results have infer that the diffusive mismatch model does not describe the trend for the thermal conductivity at these low temperatures. A frequency dependent effective mean free path for boundary scattering may need to be considered in order to more accurately describe this trend. Tests need to be performed on compacted silicon

nanowire composites at temperatures lower than 60 K and higher than 300 K in order to get a better understanding about these two distinct trends of the thermal conductivity of the nanowire composite.

There is also a need to test the effects compacting nanowires of other sizes into composites. It has already been demonstrated that a composite made of silicon nanowires of d = 190 nm exhibit thermal conductivity that is similar to that of single 115 nm nanowire. Not only were the values in the same order of magnitude as those of the single 115 nm nanowire, but the values followed a similar trend as that of the 115 nm nanowire (especially at lower temperatures). This suggests that scattering within compacted nanowire composites results in thermal conductivity values similar to smooth single crystal nanowires of smaller diameters.

This research has provided thermal conductivity data on a new type of nanocomposite material. It has also pointed out the difficulties of modeling the thermal conductivity of compacted silicon nanowire materials, especially at low temperatures. However, the thermal conductivity of this material does seem to follow the trend that had been predicted by the Monte Carlo Simulation, which merits further study of this material's behavior at higher temperatures. The compaction of silicon nanowires into a composite provides a possible new way to reduce the thermal conductivity of silicon nanowires, and fabricate a bulk material with low thermal conductivity.

APPENDIX

A1 – MatLab Codes

nanocompk.m

```
function [k_o_1] = nanocompk(k_i,d,P,T_sinw)

%Calculates thermal conductivity of nanocomposite material

%k_i: thermal conductivity of no boundary resistance material
%d: grain boundary diameter (m)
%P: sample porosity

DMM_Tdependent;

A = (k_i).^-1 + (R_b)./d; % Yang model
k_o_1 = A.^-1;

k_o_1 = ((2-P)/(2-.125*P^2))*(1-P)*k_o_1; %Meredith/Tobias model

plot(T_sinw,k_o_1,'*')

end
```

DMM_Tdependent.m

```
kb = 1.38e-23;  %Boltzmann constant
hbar=1.054571726e-34;   %Reduced Planck's constant
mode_matrix = 1:3; %(TA = 1,2; LA = 3)
wD_Along = 9.65738e13; %Debye frequency, longitudinal
wD_Atrans =6.0849e13; %Debye frequency, transverse
wD_matrix = [wD_Atrans wD_Atrans wD_Along];

vjA = [5332 5332 8970];% material A phonon speeds [TA1,TA2,LA] in m/s
vjB = [5332 5332 8970];% material B phonon speeds [TA1,TA2,LA] in m/s
alpha = sum(vjB.^-2)/(sum(vjB.^-2)+sum(vjA.^-2)); %Transmissivity
count=0;

T_matrix = T_sinw; %Temperatures (K)
nT = length(T_matrix);
h = zeros(1,nT);
h_mode = zeros(1,3);

%Calculating h for all temperatures
for T = T_matrix
count = count+1;
h_int=0;
K = 1/(8*pi^2)*hbar^2/kb/T^2*alpha;
```

```
n = 5000;

%calculating h for all modes
for mode = mode_matrix
   dw = (wD_matrix(mode)-1)/n;

      %Numerical integration for all frequencies up to wD
   for w = linspace(1,wD_matrix(mode),n);
    h_disc = vjA(mode)^-2*w^4*exp(hbar*w/kb/T)/(exp(hbar*w/kb/T)-
1)^2*dw;
    h_int = h_disc+h_int;
   end
   h_mode(mode) = K*h_int;
end
h(count) = sum(h_mode);
end

R_b = (h).^-1; %Thermal Boundary Resistance
```

A1.2 MatLab Fitting of Thermal Conductivity

dTcalcmold_SiNW_PMMA.m

```
%calculates temperature rise (dT) for each frequency and plots the
results along with the experimental values of dT and frequency. The
sample consists of three layers (PMMA, SiNW, and Epoxy Mold)

clear all;
close all;
clc;
length=1.429e-3; %heater length
Power = 0.007540962; %power input into the heater

global omega;
global k3;
global k2;
global k1;
global k3xy;
global d1 d2 d3
global b;


b=44e-6/2; %heater width / 2


load('SiNWcomp60K.txt','-ascii'); %loads experimental values of dT
and
                                  %frequency from a file
FreqExp=SiNWcomp60K(:,1);     %frequency values
```

```
dTExp=SiNWcomp60K(:,2);       %dT values

Nfreq=size(FreqExp,1);


freqarray=FreqExp;
omegaarray=freqarray*2*pi;

dSiNW=.6e-3;      %thickness of compacted Si nanowire sample
dMold = 0.1e-9;   %thickness of epoxy mold layer (under the sample)
dPMMA= 1.5e-6;    %thickness of PMMA layer (above the sample)


d3=dMold;
d2=dSiNW;
d1=dPMMA;


kMold=.2;   %thermal conductivity of epoxy mold

kSiNW = 44; %thermal conductivity of si nanowires (change to fit
            %calculated dT vs. frequency with experimental values)

kPMMA=.12;  %thermal conductivity of PMMA (change to fit
            %calculated dT vs. frequency with experimental values)

k3=kMold;
k2=kSiNW;
k1=kPMMA;
k3xy = 1;   %ratio kx/ky

%calculates dT for each frequency using the generalized formula for
2D
%conduction heating of a multilayer-film-on substrate system
%(see eq. 5.11 in chapter 5)

for i=1:1:Nfreq
    omega=omegaarray(i);
    dT=-
Power/(pi*length*k1)*quadl(@dTfuncMold_SiNW_PMMA,0.001,1e11,1e-3);
    dTarray1(i,1)=dT;
end


%plots calculated dT vs frequency on a logarithmic scale

semilogx(freqarray,abs(dTarray1),'b','LineWidth',2);
hold on;

%plots experimental dT vs frequency on a logarithmic scale
```

```
semilogx(freqarray,dTExp,'*blue')

xlabel('Frequency [Hz]','FontSize',18)
ylabel('T rise [K]','FontSize',18)
set(gca,'FontSize',15)
grid on
hold off;
```

dTfuncMold_SiNW_PMMA.m

```
%calculates the values in the integral of the generalized formula for
%2D conduction heating of a multilayer-film-on substrate system
%(see eq. 5.11 in chapter 5)

%i.e, calculates A_1 and B_1, and then integrates over the range of
%lambda



function dT=dTfuncMold_SiNW_PMMA(lambda)

global b;
global omega;
global k3;
global k2;
global k1;
global d1 d2 d3;
%%%%%%%%%%%%%%%%%%%%%%%%%%%%%%%%%%%%%%%%%%%%%%%%%%%%%%%%%%%%%%%%%%%%%%%%%%%
%Sub layer 3: Mold
density3=1.18e3;
cp3= 1500;        %Heat capacity of epoxy mold
alpha3=k3/(density3*cp3);     %Thermal diffusivity of epoxy mold
B3=sqrt((1*lambda.^2+2*i*omega/alpha3));
theta3 = B3*d3;
A3=-1./tanh(B3*d3); %A of the boundary layer, isothermal condition

%%%%%%%%%%%%%%%%%%%%%%%%%%%%%%%%%%%%%%%%%%%%%%%%%%%%%%%%%%%%%%%%%%%%%%%%%%%
% SiNWcomposite layer:
density2=1.657e3;
cp2=710;    %Heat capacity of silicon
alpha2=k2/(density2*cp2); %Thermal diffusivity of silicon

B2=sqrt(1*lambda.^2+i*2*omega./alpha2);
theta2 = B2.*d2;
term2=A3.*k3.*B3./k2./B2;
A2=(term2-tanh(theta2))./(1-term2.*tanh(theta2));

%%%%%%%%%%%%%%%%%%%%%%%%%%%%%%%%%%%%%%%%%%%%%%%%%%%%%%%%%%%%%%%%%%%%%%%%%%%
%for PMMA:
density1=1.18e3;
```

```
cp1=1500; %Heat capacity of PMMA
alpha1=k1/(density1*cp1); %Thermal diffusivity of PMMA

B1=sqrt(1*lambda.^2+i*2*omega./alpha1);
theta1 = B1.*d1;
term1=A2.*k2.*B2./k1./B1;
A1=(term1-tanh(theta1))./(1-term1.*tanh(theta1));

%Value to be integrated over lambda
dT=1./(A1.*B1).*(sin(b*lambda)).^2./(b*lambda).^2;
end
```

A.2 - Raw Data

Table A.1: Monte Carlo Simulation of thermal conductivity of compacted Si nanowire composite

T (K)	200.3488	250.2522	300.6632	350.4795	401.5421	452.1653
k(MC, 191 nm)	42.94594	42.74559	40.75941	40.62823	38.21811	35.96401

Table A.2: Measured thermal conductivity of compacted Si nanowire composite

T sample (K)	75.034	92.461	111.775	129.642	148.45	167.521
k(exp,190nm)	44	53	56	56	56	56

T sample (K)	185.685	204.533	222.784	241.382	259.747	278.071	296.702
k(exp,190nm)	53.2	51.5	48.3	47.5	47	45.5	43

Table A.3: Thermal conductivity of 190 nm Si nanowire and calculated thermal conductivity of compacted Si nanowire composite

T (K)	29.10784	34.90121	39.38147	49.59367	59.17461	69.46632	79.69298	89.35704	99.06808	109.3923	119.0672	128.8	138.5941	148.9762
k(190 nm NW)	8.356983	12.11361	20.32399	36.62064	63.31847	68.54919	79.6819	80.6822	80.18069	72.15851	77.69183	78.56477	74.05063	73.64007
k(yang, 190 nm)	2.918909	4.713368	7.149553	13.49066	22.19488	28.99183	36.49278	41.04938	44.37197	44.36113	48.46789	50.51432	49.90442	50.83075
k(analytical, 190 nm)	1.788264	2.887635	4.380159	8.265023	13.59765	17.76178	22.35723	25.14882	27.1844	27.17776	29.69376	30.9475	30.57384	31.14135
T (K)	158.7089	168.4416	178.8418	188.5817	198.971	208.711	218.4726	228.8691	238.6344	248.3707	258.7817	268.5253	278.2797	288.6834
k(190 nm NW)	76.44118	75.6119	73.77032	73.38427	72.5916	70.93819	69.2874	68.02619	65.9441	65.05385	64.01564	63.6034	62.46936	60.95786
k(yang, 190 nm)	53.05749	53.40778	53.13568	53.45105	53.49341	52.95294	52.33378	51.88802	50.8856	50.54236	50.08779	49.97897	49.40179	48.56756
k(analytical, 190 nm)	32.50556	32.72017	32.55346	32.74668	32.77263	32.44151	32.06219	31.78909	31.17496	30.96467	30.68618	30.61951	30.26591	29.75482
T (K)	299.0836	308.8525	318.6105											
k(190 nm NW)	59.88938	57.62723	57.36889											
k(yang, 190 nm)	47.98801	46.60538	46.50915											
k(analytical, 190 nm)	29.39976	28.55269	28.49373											

Table A.4: Thermal conductivity of 115 nm Si nanowire

T (K)	18.79445	24.60589	29.10784	34.90121	39.38147	44.48938	49.59367	54.06309	59.17461	64.32227	69.46632	74.567	79.69298	89.35704
k(NW,115nm)	1.63102	3.08286	5.01419	7.26815	10.16201	14.01931	18.03703	21.41216	25.10903	27.20168	29.45474	33.63288	36.68806	40.07034
T (K)	99.06808	109.3923	119.0672	128.8	138.5941	148.9762	158.7089	168.4416	178.8418	188.5817	198.971	208.711	218.4726	228.8691
k(NW,115nm)	41.36712	44.26902	47.17002	47.50426	45.11131	45.44645	45.78069	46.11493	45.64794	45.66133	45.67562	45.68901	44.73987	44.43331
T (K)	238.6344	248.3707	258.7817	268.5253	278.2797	288.6834	299.0836	308.8525	318.6105					
k(NW,115nm)	43.32374	43.49756	42.54931	42.40228	41.77398	41.14657	40.67959	39.4096	38.62088					

Table A.5: Frequency and V(3w) data

	A	B	C	D	E	F	G	H	I	J	K	L	M	N	O
2	freq	ln(freq)	300	280	260	240	220	200	180	160	140	120	100	80	60
3	5	1.609437912	0.000453634	0.00044363	0.0004345	0.00042631	0.00041929	0.00041357	0.00040996	0.0004086	0.00041005	0.00041611	0.000428801	0.000452796	0.000487564
4	5.399204136	1.68625156	0.000452796	0.00044275	0.00043383	0.00042553	0.0004186	0.00041282	0.00040948	0.00040761	0.00040924	0.00041541	0.000427775	0.000451857	0.000485802
5	5.83028106	1.763065209	0.000451846	0.00044207	0.00043277	0.00042482	0.00041792	0.00041237	0.00040859	0.00040704	0.00040859	0.00041467	0.0004269	0.000450656	0.000484368
6	6.295775523	1.839878857	0.000451062	0.00044112	0.00043221	0.00042421	0.00041722	0.00041153	0.00040769	0.00040639	0.00040795	0.00041387	0.000426233	0.000449805	0.000483019
7	6.798435448	1.916692505	0.000450172	0.00044036	0.00043136	0.00042322	0.00041631	0.00041112	0.00040705	0.00040555	0.0004073	0.00041322	0.000425469	0.000449145	0.00048179
8	7.341228158	1.993506153	0.000449564	0.00043976	0.00043069	0.00042256	0.00041569	0.00041036	0.00040651	0.0004049	0.00040669	0.00041268	0.000424728	0.000448005	0.000480417
9	7.927357887	2.070319801	0.000448901	0.00043884	0.00043019	0.00042188	0.00041516	0.00040973	0.00040602	0.0004044	0.00040596	0.00041188	0.000423845	0.000447182	0.000479223
10	8.560284698	2.147133449	0.000448216	0.00043832	0.00042926	0.00042134	0.00041444	0.00040895	0.00040526	0.0004038	0.00040533	0.00041115	0.000423426	0.000446441	0.000478208
11	9.243744909	2.223947097	0.000447555	0.0004375	0.00042855	0.00042069	0.00041391	0.00040831	0.00040456	0.00040313	0.00040472	0.00041068	0.000422662	0.000445606	0.00047705
12	9.981773149	2.300760745	0.000446858	0.00043707	0.00042808	0.00041994	0.00041331	0.00040774	0.00040407	0.00040254	0.00040414	0.00040996	0.000421939	0.0004449	0.000476036
13	10.77872617	2.377574393	0.000446321	0.00043643	0.00042755	0.00041941	0.00041254	0.00040728	0.00040332	0.00040205	0.0004036	0.00040938	0.000421466	0.000444129	0.000474911
14	11.63930859	2.454388041	0.000445521	0.00043569	0.00042684	0.00041898	0.00041204	0.00040653	0.00040292	0.00040154	0.00040295	0.00040872	0.000420811	0.000443282	0.00047409
15	12.56860061	2.531201689	0.000445034	0.00043519	0.00042632	0.00041841	0.00041153	0.00040618	0.00040244	0.00040111	0.00040245	0.00040811	0.000420231	0.000442892	0.000473088
16	13.57208808	2.608015337	0.000444569	0.00043465	0.00042604	0.00041812	0.000411	0.00040057	0.00040179	0.00040039	0.00040184	0.00040764	0.000419619	0.000442235	0.000472007
17	14.65569482	2.684828985	0.000444016	0.00043415	0.00042528	0.00041739	0.00041053	0.00040516	0.00040139	0.00039989	0.00040132	0.00040705	0.000419091	0.000441382	0.000471424
18	15.82581762	2.761642633	0.000443485	0.00043372	0.00042474	0.000417	0.00041001	0.00040456	0.00040096	0.00039955	0.00040087	0.0004067	0.000418458	0.000440907	0.00047046
19	17.08936399	2.838456281	0.000442948	0.00043327	0.00042433	0.00041655	0.00040968	0.00040418	0.0004006	0.00039893	0.00040039	0.00040602	0.000417769	0.000440242	0.000469672
20	18.45379295	2.915269929	0.000442546	0.00043274	0.00042397	0.00041604	0.00040929	0.00040381	0.00040017	0.00039856	0.00040003	0.00040563	0.00041731	0.000439586	0.000468774
21	19.92715904	2.992083577	0.000442255	0.00043055	0.00042223	0.00042043	0.00041094	0.00039955	0.00040059	0.00039903	0.00040019	0.00040779	0.00042009	0.000442689	0.000471618
22	21.5181599	3.068897225	0.000441421	0.00043166	0.00042302	0.00041514	0.00040854	0.00040291	0.00039946	0.00039774	0.00039902	0.00040491	0.000416311	0.000438318	0.00046753
23	23.23618759	3.145710873	0.000441056	0.00043141	0.00042265	0.00041479	0.00040804	0.00040252	0.00039889	0.00039739	0.00039868	0.00040426	0.000415893	0.000437878	0.000466777
24	25.09138403	3.222524521	0.000440482	0.00043096	0.00042213	0.00041427	0.00040765	0.00040236	0.00039857	0.00039702	0.00039833	0.00040392	0.000415465	0.000437384	0.000465999
25	27.09470088	3.299338169	0.000440074	0.0004303	0.00042183	0.00041384	0.00040729	0.00040182	0.00039806	0.00039685	0.00039798	0.00040351	0.000414824	0.000436857	0.000465363
26	29.25796421	3.376151817	0.000439603	0.00043005	0.00042128	0.0004137	0.00040676	0.00040157	0.00039792	0.00039628	0.00039763	0.00040316	0.000414552	0.000436308	0.000464832
27	31.59394428	3.452965465	0.000438957	0.00042954	0.00042081	0.00041316	0.00040641	0.00040108	0.00039743	0.00039584	0.00039712	0.0004028	0.000414265	0.0004357	0.000464307
28	34.11643092	3.529779113	0.000438405	0.00042911	0.00042046	0.00041268	0.00040609	0.00040071	0.00039971	0.00039549	0.00039679	0.00040248	0.000413848	0.00043544	0.000463791
29	36.84031499	3.606592761	0.000438061	0.00042841	0.00041993	0.00041229	0.00040572	0.00040025	0.0003967	0.00039513	0.00039655	0.00040215	0.000413397	0.000435034	0.000463218
30	39.78167621	3.68340641	0.00043731	0.00042818	0.00041911	0.00041124	0.00040526	0.0004002	0.00039579	0.00039458	0.00039585	0.00040197	0.000413338	0.000434399	0.00046307
31	42.95787814	3.760220058	0.000436939	0.00042761	0.00041901	0.00041142	0.00040477	0.00039963	0.00039599	0.00039458	0.00039601	0.00040135	0.000412775	0.000434378	0.000462143
32	46.38767067	3.837033706	0.000436386	0.00042703	0.00041849	0.00041114	0.00040448	0.00039914	0.00039563	0.00039413	0.00039558	0.00040109	0.00041246	0.000433898	0.000461759
33	50.09130067	3.913847354	0.000435641	0.00042647	0.00041801	0.00041053	0.00040399	0.00039881	0.00039531	0.00039383	0.00039524	0.00040056	0.000412036	0.000433601	0.000461323
34	54.09063155	3.990661002	0.000435125	0.00042592	0.00041758	0.00041014	0.00040359	0.00039856	0.00039494	0.00039353	0.00039503	0.00040036	0.00041725	0.00043314	0.000460818
35	58.40927231	4.06747465	0.000434555	0.00042525	0.000417	0.0004096	0.00040315	0.00039798	0.00039453	0.00039309	0.00039456	0.00040011	0.000411449	0.000432825	0.000460358
36	63.07271693	4.144288298	0.000433937	0.0004248	0.00041642	0.00040913	0.00040271	0.00039761	0.00039411	0.00039282	0.00039417	0.00039969	0.000411138	0.000432467	0.000460031
37	68.10849482	4.221101946	0.000433328	0.00042419	0.00041595	0.00040861	0.0004022	0.00039718	0.00039373	0.00039249	0.00039391	0.00039947	0.000410671	0.000432076	0.000459636
38	73.54633339	4.297915594	0.000432689	0.00042354	0.00041533	0.00040788	0.00040179	0.00039683	0.00039339	0.00039191	0.00039363	0.00039904	0.000410328	0.000431718	0.000459077
39	79.41833348	4.374729242	0.000432147	0.00042294	0.00041483	0.00040756	0.00040119	0.00039619	0.00039288	0.00039156	0.00039315	0.00039862	0.000410011	0.000431398	0.000458825
40	85.75915892	4.45154289	0.00043131	0.00042233	0.00041425	0.00040692	0.00040078	0.00039577	0.00039238	0.00039119	0.00039267	0.0003982	0.000409635	0.00043079	0.000458324
41	92.60624111	4.528356538	0.000430645	0.00042165	0.00041355	0.0004064	0.00040018	0.00039524	0.00039199	0.00039068	0.0003923	0.00039792	0.00040915	0.0004305	0.00045793
42	100	4.605170186	0.000429571	0.00042234	0.00041157	0.00040619	0.00040058	0.00039569	0.00039269	0.00039063	0.00039298	0.00039813	0.000409847	0.00042916	0.000456365
43	107.9840827	4.681983834	0.000429448	0.00042048	0.00041255	0.00040524	0.00039926	0.00039425	0.00039108	0.00038986	0.00039149	0.00039711	0.000408473	0.00042979	0.000456872
44	116.6056212	4.758797482	0.000428669	0.00041984	0.00041181	0.00040477	0.00039858	0.00039373	0.00039065	0.00038948	0.00039115	0.00039664	0.000408098	0.00042933	0.000456514
45	125.9155105	4.83561113	0.00042806	0.00041916	0.00041131	0.00040412	0.00039796	0.00039323	0.00039301	0.00038892	0.00039071	0.00039623	0.000407651	0.00042852	0.000456091
46	135.968709	4.912424778	0.000427339	0.00041852	0.00041056	0.00040353	0.00039745	0.00039268	0.00038965	0.00038859	0.00039017	0.00039586	0.000407189	0.00042859	0.000455501
47	146.8245632	4.989238426	0.000426581	0.00041783	0.00041008	0.00040298	0.00039702	0.00039226	0.00038904	0.00038808	0.00038968	0.00039549	0.000406744	0.00042802	0.000455024
48	158.5471577	5.066052074	0.000425911	0.00041712	0.00040931	0.00040242	0.00039635	0.00039173	0.00038858	0.00038753	0.00038934	0.00039505	0.000406422	0.00042759	0.0004545
49	171.205694	5.142865722	0.000425234	0.00041636	0.00040873	0.00040171	0.00039577	0.00039106	0.00038793	0.000387	0.00038868	0.0003946	0.000406086	0.00042729	0.00045391
50	184.8748982	5.21967937	0.000424439	0.00041589	0.00040817	0.0004013	0.00039521	0.0003906	0.00038755	0.00038649	0.00038839	0.00039411	0.000405552	0.00042658	0.00045346
51	199.635463	5.296493018	0.000423761	0.00041518	0.00040747	0.00040063	0.0003946	0.00039005	0.000387	0.00038598	0.00038785	0.00039363	0.000405034	0.00042617	0.00045264
52	215.5745235	5.373306666	0.000422986	0.00041439	0.00040674	0.00039991	0.00039399	0.00038948	0.00038647	0.00038543	0.00038741	0.00039308	0.000404472	0.00042578	0.00045205
53	232.7861718	5.450120314	0.000422129	0.00041383	0.0004061	0.00039938	0.00039352	0.00038892	0.00038592	0.00038509	0.00038681	0.00039268	0.000404036	0.00042538	0.00045153
54	251.3720123	5.526933962	0.000421543	0.00041294	0.00040539	0.00039876	0.00039293	0.00038838	0.00038542	0.00038445	0.00038642	0.00039221	0.0004036	0.00042469	0.00045082
55	271.4417617	5.603747611	0.000420751	0.00041232	0.00040467	0.00039822	0.00039232	0.0003878	0.00038478	0.00038407	0.00038586	0.00039167	0.000402991	0.00042411	0.00045073
56	293.1138964	5.680561259	0.000419978	0.00041154	0.00040415	0.00039742	0.00039172	0.00038721	0.00038424	0.00038347	0.00038535	0.00039104	0.000402527	0.00042379	0.00044936
57	316.5163524	5.757374907	0.000419123	0.00041092	0.00040329	0.00039685	0.00039118	0.00038669	0.0003837	0.00038289	0.00038485	0.00039062	0.000401963	0.00042346	0.00044901
58	341.7872798	5.834188555	0.000418447	0.00041026	0.00040276	0.00039621	0.00039039	0.00038607	0.00038307	0.00038243	0.00038427	0.00039008	0.000401389	0.0004225	0.00044869
59	369.0758589	5.911002203	0.000417529	0.00040945	0.00040212	0.00039553	0.00038982	0.00038541	0.00038261	0.00038191	0.00038381	0.00038963	0.000400962	0.00042187	0.00044729
60	398.5431808	5.987815851	0.000416743	0.00040878	0.00040125	0.0003949	0.00038922	0.00038496	0.00038202	0.00038129	0.00038315	0.00038908	0.000400486	0.00042143	0.0004466
61	430.363198	6.064629499	0.000415983	0.00040794	0.00040055	0.00039422	0.00038866	0.00038439	0.0003815	0.00038073	0.00038271	0.0003887	0.000399979	0.00042081	0.00044591
62	464.7237517	6.141443147	0.000415226	0.0004071	0.00039994	0.00039351	0.00038804	0.00038356	0.00038099	0.00038016	0.00038217	0.00038807	0.000399346	0.00042022	0.00044517
63	501.8276805	6.218256795	0.000414195	0.00040632	0.000399	0.00039262	0.00038709	0.00038306	0.00038028	0.00037957	0.00038163	0.00038751	0.000398701	0.00041955	0.00044429
64	541.8940176	6.295070443	0.000413274	0.00040555	0.00039828	0.000392	0.00038643	0.00038225	0.00037973	0.000379	0.00038097	0.00038696	0.000398271	0.00041898	0.00044319
65	585.1592842	6.371884091	0.000412539	0.00040463	0.00039752	0.00039119	0.00038583	0.00038152	0.00037915	0.00037843	0.0003805	0.00038624	0.00039758	0.00041841	0.00044283
66	631.8788855	6.448697739	0.00041163	0.00040378	0.00039675	0.00039043	0.00038505	0.00038098	0.00037833	0.00037769	0.00037986	0.00038564	0.000396993	0.00041799	0.0044203
67	682.3286184	6.525511387	0.00041029	0.00040285	0.00039583	0.00038954	0.00038437	0.00038028	0.00037763	0.00037702	0.00037919	0.00038507	0.000396423	0.00041752	0.00044121
68	736.8062997	6.602325035	0.000409534	0.00040179	0.00039492	0.00038865	0.00038339	0.00037943	0.00037665	0.00037649	0.0003784	0.00038451	0.0003973	0.00041681	0.00044059
69	795.6335242	6.679138683	0.000408413	0.00040082	0.00039393	0.00038774	0.00038271	0.00037861	0.00037623	0.00037571	0.00037779	0.00038371	0.000394978	0.00041615	0.00043506
70	859.1575629	6.755952331	0.000407038	0.00039981	0.00039321	0.00038725	0.00038171	0.0003778	0.00037539	0.00037513	0.00037696	0.00038324	0.000394305	0.00041558	0.00043767
71	927.7534134	6.832765979	0.000406141	0.00039865	0.00039202	0.000386	0.00038088	0.00037698	0.00037456	0.00037405	0.00037632	0.00038225	0.000393655	0.00041137	0.0043756
72	1001.826013	6.909579627	0.000404879	0.00039752	0.00039083	0.0003849	0.00037986	0.00037605	0.00037374	0.0003732	0.00037543	0.00038146	0.000392878	0.00041317	0.00043725
73	1081.812631	6.986393275	0.00040352	0.00039617	0.0003897	0.00038389	0.00037902	0.00037515	0.00037281	0.00037239	0.00037462	0.00038076	0.000392014	0.00041526	0.00043561
74	1168.185446	7.063206923	0.000402154	0.00039486	0.00038844	0.00038278	0.00037779	0.00037402	0.00037176	0.00037155	0.00037383	0.00037988	0.000391146	0.00041572	0.00043609
75	1261.454339	7.140020571	0.000400541	0.00039347	0.00038707	0.00038138	0.00037653	0.00037297	0.00037069	0.00037055	0.00037281	0.00037887	0.000390152	0.0004106	0.00043577
76	1362.169896	7.216834219	0.000398973	0.00039185	0.00038575	0.00037998	0.0003754	0.00037176	0.00036961	0.00036933	0.00037173	0.00037781	0.000389129	0.00040954	0.00043249
77	1470.926668	7.293647867	0.000397211	0.00039038	0.00038412	0.00037862	0.00037403	0.00037047	0.00036842	0.00036825	0.00037067	0.00037676	0.000388105	0.00040849	0.00043130
78	1588.36667	7.370461515	0.000395814	0.0003887	0.00038248	0.000377	0.00037242	0.00036903	0.00036715	0.00036697	0.00036949	0.0003756	0.00038603	0.00040724	0.00043022
79	1715.183178	7.447275163	0.000393601	0.00038788	0.00038139	0.00037562	0.00037096	0.00036756	0.00036573	0.00036568	0.00036816	0.00037437	0.000385696	0.00040597	0.00042878
80	1852.124822	7.524088812	0.000403835	0.00039488	0.00038192	0.00037477	0.00036967	0.00036609	0.00036417	0.0003642	0.00036675	0.00037297	0.00038439	0.00040452	0.00042829
81	2000	7.60090246	0.000454854	0.00043115	0.00040076	0.00038012	0.00037024	0.00036547	0.00036282	0.0003626	0.00036517	0.00037144	0.00038292	0.00040305	0.0042662

Table A.6: Data for Slope and Curve Fitting Method

85	set point T controller	300	280	260	240	220	200	180	160	140	120	100	80	60
86	T from Tcont at low	300.01	279.97	260.01	240.01	220	200.01	179.99	159.99	140.03	119.99	99.975	79.992	59.959
87	R at low (Rset methoc	15.858776	15.446007	15.036192	14.625405	14.211863	13.797114	13.379746	12.959874	12.535474	12.106134	11.681672	11.231039	10.769474
88	T from Tcont at high	299.98	280	260.01	240.01	220.02	200.02	180	160	140	120	100.02	80.001	59.995
89	R at high (Rset metho	16.126025	15.716928	15.310284	14.902618	14.492621	14.080821	13.668447	13.254364	12.836571	12.415491	12.000802	11.563735	11.206488
90	V(A-B) at high	0.000046	0.000145	0.000046	0.000038	0.000099	0.00013	0.000145	0.000099	0.000099	0.000137	0.000069	0.000061	0.000031
91	V1w at high	0.417317	0.406819	0.396279	0.385728	0.375116	0.364456	0.3538	0.343083	0.332263	0.321368	0.310624	0.299283	0.290037
92	some T measurement	300.03	280.02	260.02	240	220.01	200	179.98	159.99	140.02	120.02	99.997	79.982	59.945
93	Tsample 1st	291.958	273.261	254.572	235.692	217.169	198.446	179.264	160.754	141.51	122.509	104.253	84.795	-9.9E+37
94	I low	0.005	0.005	0.005	0.005	0.005	0.005	0.005	0.005	0.005	0.005	0.005	0.005	0.005
95	I sweep	0.026	0.026	0.026	0.026	0.026	0.026	0.026	0.026	0.026	0.026	0.026	0.026	0.026
96	I high	0.026	0.026	0.026	0.026	0.026	0.026	0.026	0.026	0.026	0.026	0.026	0.026	0.026
97	TC voltage 1st	-0.000315	-0.00107	-0.001794	-0.002511	-0.003174	-0.003826	-0.004446	-0.005012	-0.005553	-0.006032	-0.006436	-0.006826	-0.007131
98	T ref junction 1st	299.79844	299.98594	299.93906	300.04844	299.92344	300.17344	300.17344	300.36875	300.61094	300.70469	300.73594	301.2125	300.86094
99	V(B) high	0.52686	0.526975	0.526956	0.526957	0.526957	0.526955	0.526981	0.526983	0.526974	0.526981	0.526964	0.526915	0.526915
100	Rset	20.359	20.359	20.359	20.359	20.359	20.359	20.359	20.359	20.359	20.359	20.359	20.359	20.359
101	Rlow (V/I)	15.798441	15.392101	14.982076	14.571836	14.162346	13.747148	13.333377	12.913747	12.491714	12.064698	11.641735	11.192068	10.732196
102	Rhigh (V/I)	16.050463	15.646695	15.241327	14.835528	14.427372	14.017365	13.607514	13.195328	12.779175	12.360141	11.946917	11.510757	11.155147
103	Tsample 2nd	296.702	278.071	259.747	241.382	222.784	204.533	185.685	167.521	148.45	129.642	111.775	92.461	75.034
104	TC voltage 2nd	-0.000124	-0.000878	-0.001594	-0.002299	-0.002974	-0.003622	-0.004244	-0.004814	-0.005366	-0.005858	-0.006276	-0.006685	-0.006975
105	T ref junction 2nd	299.79844	299.98594	299.97031	300.04844	299.92344	300.17344	300.17344	300.42344	300.61094	300.67344	300.73594	301.17344	300.92344
106	Tsample 3rd	297.613	279.212	260.901	242.426	224.033	205.482	187.031	168.602	148.975	130.796	112.324	92.667	74.941
107	TC voltage 3rd	-0.000091	-0.000831	-0.001553	-0.002257	-0.002934	-0.003591	-0.004205	-0.004781	-0.005356	-0.005836	-0.00627	-0.006684	-0.006963
108	T ref junction 3rd	299.86094	299.92344	300.00156	299.92344	300.04844	300.23594	300.28281	300.4	300.67344	300.79844	300.86094	301.23594	300.61094
109	power	0.010850242	0.0105773	0.0103033	0.0100289	0.009753	0.0094759	0.0091988	0.0089202	0.0086388	0.0083556	0.00807622	0.00778136	0.00754096
110	dR/dT	0.022182731	0.0221827	0.0221827	0.0221827	0.0221827	0.0221827	0.0221827	0.0221827	0.0221827	0.0221827	0.02218273	0.02218273	0.02218273
111	TCR	0.001382062	0.0014177	0.0014554	0.0014952	0.0015375	0.0015825	0.0016302	0.0016811	0.0017359	0.0017947	0.00185677	0.00192713	0.00198856
112	slope	-9.5762E-06	-9.22E-06	-8.29E-06	-8.01E-06	-7.75E-06	-7.33E-06	-7.16E-06	-6.63E-06	-6.55E-06	-6.25E-06	-6.35E-06	-6.253E-06	-7.727E-06
113	length	0.001429	0.001429	0.001429	0.001429	0.001429	0.001429	0.001429	0.001429	0.001429	0.001429	0.001429	0.001429	0.001429
114	k	36.39148567	36.849241	39.895179	40.19458	40.417349	41.545271	41.24201	43.201938	42.387609	42.912279	40.8495835	39.9678895	31.3454647

Notes:

1. Green highlights - measured values
2. Orange highlights – calculated values from green highlights
3. Yellow highlights – slope method thermal conductivity

REFERENCES

[1] Jie Wu, Xuezheng Wei, Nitin P. Padture, Paul G. Klemens, Maurice Gell, Eugenio Garcıa, Pilar Miranzo, and Maria I. Osendi, "Low-Thermal-Conductivity Rare-Earth Zirconates for Potential Thermal-Barrier-Coating Applications," *Journa of American Ceramic Society*, Vol. 85, Issue 2, 3031–35, 2002.

[2] Chang-Lin Tien, Arunava Majumdar, Frank M. Gerner, *Microscale Energy Transport*, Washington D.C.: Taylor & Francis, 1998.

[3] C.B. Sobhan, G.P. Peterson, *Microscale and Nanoscale Heat Transfer: Fundamentals and Engineering Applications*, Boca Raton, FL: CRC Press/ Taylor & Francis, 2008.

[4] Gang Chen, *Nanoscale Energy Transport and Conversion: A Parallel Treatment of Electrons, Molecules, Phonons, and Photons*, New York, NY: Oxford University Press, 2005.

[5] Charles Kittel, *Introduction to Solid State Physics*, 7th edition, Hoboken, NJ: John Wiley & Sons, 1996.

[6] Chang-Lin Tien, Gang Chen, "Challenges in Microscale Conductive and Radiative Heat Transfer", *Journal of Heat Transfer*, Vol. 116, pp. 799 – 807, 1994.

[7] M.I. Flik, B.I. Choi, & K.E. Goodson, "Heat Transfer Regimes in Microstructures," *Journal of Heat Transfer*, Vol.114, pp. 666 – 674, 1992.

[8] David G. Cahill, Wayne K. Ford, Kenneth E. Goodson, Gerald D. Mahan, Arun Majumdar, Humphrey J. Maris, Roberto Merlin, Simon R. Phillpot, "Nanoscale Thermal Transport", *Journal of Applied Physics*, Vol. 93, Iss. 2, pp. 793 – 818, 2003.

[9] E.T. Swartz, R.O. Pohl, "Thermal Boundary Resistance", *Reviews of Modern Physics*, Vol. 61, No. 3, pp. 605 – 658, 1989.

[10] P. Sheng, *Introduction to Wave Scattering, Localization and Mesoscopic Phenomenon*, 2nd ed., Berlin, Germany: Springer-Verlag, 2006.

[11] Deyu Li, Yiying Wu, Philip Kim, Li Shi, Peidong Yang, Arun Majumdara, "Thermal Conductivity of Individual Nanowires," *Applied Physics Letters*, Vol. 83, No. 14, 2003

[12] Allon I. Hochbaum, Renkun Chen, Raul Diaz Delgado, Wenjie Liang, Erik C. Garnett, Mark Najarian, Arun Majumdar, & Peidong Yang, "Enhanced Thermoelectric Performance of Rough Silicon Nanowires", *Nature*, Vol. 451, pp. 163 – 168, 2007.

[13] Yong-Hee Park, Jungwon Kim, Hyoungjoon Kim, Ilsoo Kim, Ki-Young Lee, Dongjea Seo, Heon-Jin Choi, Woochul Kim, "Thermal conductivity of VLS-grown rough Si nanowires with various surface roughnesses and diameters," *Applied Physics A*, Vol 104, pp. 7–14, 2011.

[14] Rama Venkatasubramanian, "Lattice Thermal Conductivity Reduction and Phonon Localizationlike Behavior in Superlattice Structures," *Physical Review B*, Vol. 61, No. 4, pp. 3091 – 3097.

[15] Maria N. Luckyanova, Jivtesh Garg, Keivan Esfarjani, Adam Jandl, Mayank T. Bulsara, Aaron J. Schmidt, Austin J. Minich, Shuo Chen, Mildred S. Dresselhaus, Zhifeng Ren, Eugene A. Fitzgerald, Gang Chen, "Coherent Phonon Heat Conduction in Superlattices," *Science,*Vol 338, 2012.

[16] X.W. Wang, H. Lee, Y.C. Lan, G.H. Zhu, G. Joshi, D.Z. Wang, J. Yang, A.J. Muto, M.Y. Tang, J. Klatsky, S. Song, M.S. Dresselhaus, G. Chen, and Z. F. Ren, "Enhanced thermoelectric figure of merit in nanostructured n-type silicon germanium bulk alloy," *Applied Physics Letters*, Vol. 93, 2008.

[17] Ce-Wen Nan, R. Birringer, David R. Clarke, H. Gleiter, "Effective Thermal Conductivity of Particulate Composites with Interfacial Thermal Resistance," *Journal of Applied Physics*, Vol. 81, No. 10, pp. 6692 – 6699, 1997.

[18] Ho-Soon Yang, G.-R. Bai, L.J. Thompson, J.A. Eastman, "Interfacial Thermal Resistance in Nanocrystalline Yttria-stabilized Zirconia," *Acta Materialia*, Vol. 50, pp. 2309 – 2317, 2002.

[19] Jay Amrit, "Grain Boundary Kapitza Resistance and Grain-arrangement Induced Anisotropy in the Thermal Conductivity of Polycrystalline Niobium at Low Temperatures," *Journal of Physics D: Applied Physics*, Vol. 39, pp. 4472-4477, 2006

[20] T. H. Bauer, "A General Analytical Approach Toward the Thermal Conductivity of Porous Media," *International Journal of Heat Mass Transfer*, Vol. 36, No. 17, pp. 4181-4191, 1993.

[21] F. Cernuschi, S. Ahmaniemi, P. Vuoristo, T. Mantyla, "Modeling of Thermal Conductivity of Porous Materials: Application to Thick Barrier Coatings," *Journal of the European Ceramic Society*, Vol. 24, pp. 2657-2667, 2004.

[22] David S. Mclachian, Michael Biaszkiewicz, and Robert E. Newnham, "Electrical Resistivity of Composites," *Journal of American Chemistry Society*, Vol. 73, No. 8, pp. 2187 – 2203, 1990.

[23] Haiyu Fang, Tianli Feng, Haoran Yang, Xiulin Ruan, and Yue Wu, "Synthesis and Thermoelectric Properties of Compositional-Modulated Lead Telluride-Bismuth Telluride Nanowire Heterostructures," *Nano Letters*, Recently Accepted, 2013.

[24] Weixue Tian and Ronggui Yang, "Thermal Conductivity Modeling of Compacted Nanowire Composites," *Journal of Applied Physics*, Vol. 101, 2007.

[25] Ming-Shan Jeng, Ronggui Yang, and Gang Chen, "Monte Carlo Simulation of Thermoelectric Properties of Nanocomposites," *Journal of Heat Transfer*, 2005.

[26] Joseph P. Feser, "Scalable Routes to Efficient Thermoelectric Materials," Doctoral Dissertation, University of California, Berkley, 2010.

[27] David G. Cahill, "Thermal Conductivity Measurement from 30 to 750K: The 3ω Method," *Review of Scientific Instrumentation*, Vol 61, No. 2, 1990.

[28] T. Borca-Tasciuc, A.R. Kumar, and G. Chen, "Data Reduction in 3ω Method for Thin-film Thermal Conductivity Determination," *Review of Scientific Instruments*, Vol. 72, No. 4, pp. 2139-2147, 2001.

[29] Zhaojie Wang, Joseph E. Alaniz, Wanyoung Jang, Javier E. Garay, and Chris Dames, "Thermal Conductivity of Nanocrystalline Silicon: Importance of Grain Size and Frequency-Dependent Mean Free Paths," *Nano Letters*, Vol. 11, pp. 2206 – 2213, 2011.

[30] Mei-Jiau Huang, Wen-Yen Chong, and Tai-Ming Chang, "The Lattice Thermal Conductivity of a Semiconductor Nanowire," *Journal of Applied Physics*, Vol. 99, No. 114318, 2006.

[31] W.S. Capinski, H.J, Maris, "Thermal Conductivity of GaAs/AsAl Superlattices," *Physica B: Condensed Matter*, Vol. 219-220, 1996.

[32] J. Anaya, J. Jiménez and T. Rodríguez, "Thermal Transport in Semiconductor Nanowires," *Nanowires-Recent Advances*, pp. 231-260, 2012.

[33] C.J. Glassbrenner and Glen A. Slack, "Thermal Conductivity of Silicon and Germanium from 3K to the Melting Point," *Physical Review,* Vol. 134, No. 4A, pp. A1058 – A1069, 1963.

[34] D.J. Jeffery, "Conduction through a Random Suspension of Spheres," *Proceedings of The Royal Society London A,* Vol. 335, pp. 335-367, 1973.